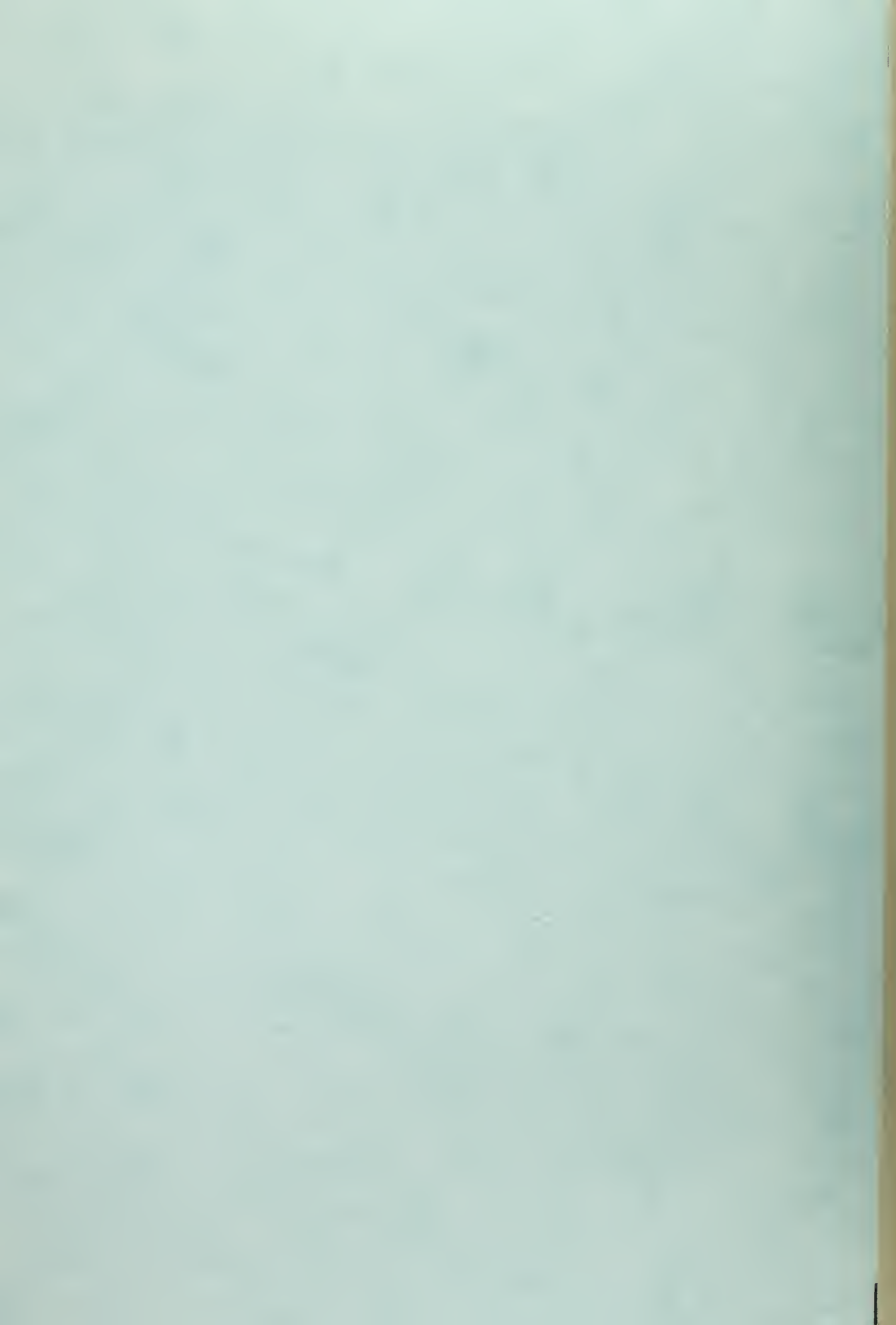


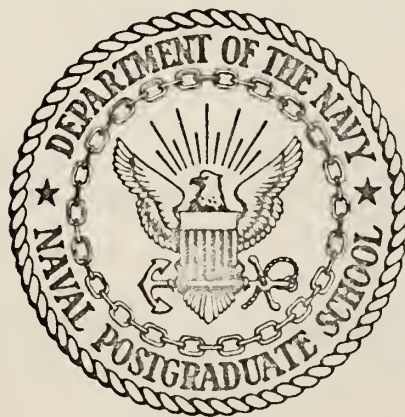
AN OCEAN FORECASTING MODEL
FOR THE EQUATORIAL REGION

Byron Richard Maxwell



NAVAL POSTGRADUATE SCHOOL

Monterey, California



THESIS

AN OCEAN FORECASTING MODEL
FOR THE EQUATORIAL REGION

by

Byron Richard Maxwell

Thesis Advisor:

R. L. Haney

September 1972

Approved for public release; distribution unlimited.

T152296

LIBRARY
NAVAL POSTGRADUATE SCHOOL
MONTEREY, CALIF. 93940 /

An Ocean Forecasting Model
for the Equatorial Region

by

Byron Richard Maxwell
Lieutenant, United States Navy
B.S., University of Oregon, 1965

Submitted in partial fulfillment of the
requirements for the degree of

MASTER OF SCIENCE IN METEOROLOGY

from the

NAVAL POSTGRADUATE SCHOOL
September 1972

ABSTRACT

A seven level primitive equation equatorial ocean model with temperature and salinity is integrated over a 30 year period to a quasi-steady state. Placement of four of the seven levels of the model in the first 100 meters gives sufficient vertical resolution to resolve most major features of equatorial oceans. The model equivalents of the South Equatorial Current, the Cromwell Current, vertical upwelling in the equatorial area, Ekman divergence of mass toward each pole, and a thermocline were all simulated.

A major conclusion was salinity probably has little effect on the general circulation patterns in the equatorial region. Additionally, the use of a vertical eddy diffusion coefficient for momentum that is dependent upon vertical stability, vertical current shear, and depth will probably be required to accurately model the vertical structure of the currents.

TABLE OF CONTENTS

I.	INTRODUCTION -----	9
II.	DESIGN OF THE MODEL -----	12
	A. MATHEMATICAL STATEMENT OF THE PROBLEM -----	12
	B. HORIZONTAL AND VERTICAL FINITE DIFFERENCING --	23
	1. The Horizontal Grid -----	23
	2. Differencing of Horizontal Advection -----	25
	3. Differencing of Horizontal Diffusion -----	27
	4. The Vertical Grid -----	29
	5. Finite Differencing of Vertical Advection-	31
	6. Differencing of Vertical Diffusion -----	32
	C. EQUATION OF STATE -----	35
	1. Density as a Function of Temperature and Salinity -----	35
	2. Solution for α and β -----	37
	D. INSTANTANEOUS CONVECTIVE ADJUSTMENT OF DENSITY -----	38
III.	RESULTS -----	46
	A. THE TIME DEPENDENT BEHAVIOR OF THE MODEL -----	46
	1. Salinity Relaxation Time -----	46
	2. Temperature Relaxation Time -----	53
	3. Dynamic Current Relaxation Time -----	56
	B. EQUATORIAL UNDERCURRENT -----	60
	C. CURRENT CIRCULATIONS -----	72
	D. THERMAL STRUCTURE -----	77
	E. SALINITY STRUCTURE -----	82
	F. DENSITY STRUCTURE -----	85
	G. MASS TRANSPORT -----	87

IV. CONCLUSIONS -----	89
LIST OF REFERENCES -----	90
INITIAL DISTRIBUTION LIST -----	92
FORM DD 1473 -----	95

LIST OF FIGURES

Figure		Page
2.1	Horizontal domain of the model -----	13
2.2	Vertical structure of the model showing seven levels with dense packing near the surface -----	14
2.3	The annual latitudinal mean zonal stress for all oceans combined after Hellerman (1967) -----	18
2.4	The atmospheric surface air temperature and heat flux components Q_1 and Q_2 -----	19
2.5	Evaporation and precipitation rates after Budyko (1963) -----	21
2.6	The horizontal space staggered grid -----	24
2.7	The west wall used to derive the finite difference analogues along the boundary at the general grid point (l,j) -----	24
2.8	Location of the variables in the vertical grid -----	30
2.9	Plot of sigma-t vs. temperature and salinity, after Von Arx (1964) -----	36
2.10	Stable density profile -----	40
2.11	Model equivalent of the stable density profile -----	40
2.12	Diagram of an unstable state due to the temperature profile showing the necessary temperature adjustments to achieve stability -----	42
3.1	A plot of S^* vs. $\tau = \tau / (2\sqrt{kt})$ -----	50
3.2	A plot of salinity vs. time at the grid point with maximum upward surface flux for levels 5, 20, 100, 250, and 700 meters -----	52

3.3	Temperature vs. time plots for levels 5, 20, 100, 250, and 700 meters over a 30 year period -----	55
3.4	A plot of zonal current vs. time at the grid point I = 10, J = 9 located on the equator midway between the east and west boundaries. The depth is 20 meters -----	57
3.5	Zonal current $u(\text{cm/sec})$ vs. time at grid point I = 10, J = 9 at 100 meters -----	58
3.6	Zonal current $u(\text{cm/sec})$ vs. time at grid point I = 10, J = 9 at 700 meters -----	59
3.7	(After Veronis) A cellular circulation develops when a nonrotating basin is subjected to a surface wind stress -----	62
3.8	E-W cross section along the equator of $u(\text{cm/sec})$ vs. depth (meters) after 30 years of integration -----	64
3.9	E-W cross section of zonal current (cm/sec) along the equator in the Pacific Ocean after Knauss (1960) -----	65
3.10	Plot comparing the average model zonal current with the smoothed zonal current at 118 W in the eastern tropical Pacific as determined by Knauss (1966). The model time is 30 years -----	67
3.11	A N-S vertical cross section of zonal current at a location midway between the eastern and western boundaries at 30 years of time integration. The undercurrent is centered on the equator, where the horizontal velocity (u, v) is calculated -----	69
3.12	N-S cross section of zonal current and the associated thermal structure at 140 W for 20-22 April 1958 after Knauss -----	70
3.13	N-S cross section of temperature at the midpoint between the eastern and western boundaries -----	71

3.14	Horizontal cross section of zonal current (cm/sec) at a depth of 5 m after 30 years of time integration -----	74
3.15	Horizontal cross section of meridional current v (cm/sec) at 5 meters after 30 years -----	75
3.16	Horizontal cross section of vertical velocity w (cm/sec) after 30 years -----	76
3.17	A horizontal cross section of temperature (°C) at 5 meters -----	78
3.18	An E-W vertical cross section of temperature (°C) along the equator for contour interval 0.5°C. The vertical lines are soundings plotted in figure 3.19. These three stations give a detailed look at the vertical thermal structure -----	80
3.19	Vertical temperature profiles at three selected stations along the equator as marked on figure 3.18 -----	81
3.20	Horizontal cross section of salinity anomaly ($S\text{‰} - 34.5\text{‰}$) x 100 at 5 m after 30 years -----	83
3.21	An E-W equatorial vertical cross section of salinity anomaly ($S\text{‰} - 34.5\text{‰}$) x 100 -----	84
3.22	An equatorial E-W cross section of density anomaly ($\rho - 1.0$) x 1000 -----	86
3.23	The transport streamfunction -----	88

ACKNOWLEDGEMENTS

I wish to express my gratitude to Professor Robert L. Haney for his infinite patience and expert guidance during all portions of the work, and Professor Russell L. Elsberry for his careful scrutiny of the final manuscript.

I am grateful for the generous assistance provided by the staff of the William R. Church Computer Center of the Naval Postgraduate School, especially the swing shift and night crews. All programming was done on the IBM 360/67 Computer located in this computer center.

Finally, I wish to express my appreciation to my wife and family for their moral support during critical phases of my work.

I. INTRODUCTION

Numerical baroclinic ocean models are advancing to the state where oceanic forecasting may become feasible. The motivation for the development of sophisticated ocean models stems largely from the need to accurately specify the lower boundary conditions for baroclinic atmospheric models used in long-range weather prediction. The importance of the ocean in determining global climate is underscored in a recent pioneering work by Manabe (1969) and Bryan (1969) in which numerical ocean and atmospheric models were coupled together allowing interaction between the two. By comparing the results of the ocean-air model with those from an atmospheric model with a static ocean, they found the ocean plays an important role in the poleward transport of heat and helps determine the thermal structure and vertical wind shear of the troposphere. Additionally, they found that the ocean affects the hydrology of the tropics and influences the strength of the Hadley circulation. The important role of the ocean in influencing the transient behavior of the atmosphere has been recently shown by Lambertson (1972) in a coupled ocean-atmospheric model. Because of the demonstrated importance of the ocean in determining the climate and the variability of the atmosphere, and since atmospheric models are more highly developed than their ocean counterparts, it is clear that future improvement in long-range weather prediction is closely linked with the development of better ocean models.

Early oceanic prediction models were one-dimensional in the vertical with the net heat flux and, in some cases, the wind velocity or stress being specified at the surface. The thermal structure was assumed to be known initially and responded to changes in the rates of surface heating. The depth of the surface layer was determined by a mechanical energy balance, and integration of the thermodynamic equation gave the thermal profile at a later time. Although adequate for very short range purposes, these one-dimensional models are not satisfactory for long range predictions because no mechanisms for horizontal advection or diffusion of heat or momentum are present. Any location where the climatological yearly heat flux is not zero will display either a continual warming or cooling trend. Tropical areas would continue to warm and middle latitude areas would continue to cool. For long term predictions, therefore, ocean models based on heat balances alone will not be satisfactory.

Although Bryan's dynamical ocean model is adequate for the purpose of global climate investigation, it is believed that the horizontal grid spacing of 5° longitude and 5° latitude and a vertical spacing where the first level is at 67 meters is too coarse for adequate oceanic forecasting purposes. One strong point of the present model is felt to be its superior horizontal resolution of 2.5° latitude and 3.0° longitude and good vertical resolution where four of its seven levels are in the first 100 meters.

Because of the importance of equatorial air-sea interaction (Bjerknes, 1966) and the interesting oceanographic phenomena that occur in the equatorial region, it was decided to model the equatorial domain. The large vertical current shears and sharp thermocline which exist in the tropics should be simulated by an ocean model that is to be used with an atmospheric forecasting model.

II. DESIGN OF THE MODEL

A. MATHEMATICAL STATEMENT OF PROBLEM

The idealized domain is 60° wide, extends from 21.25 S to 21.25 N, and has a uniform depth of 3000 meters. Placement of the lateral walls at approximately 20° latitude in both hemispheres satisfies two important requirements: first, the curl of the observed wind stress is almost zero at these locations; and second, the area averaged flux of salt as determined from climatological evaporation and precipitation data is approximately zero when averaged from 21.25 S to 21.25 N. Seven vertical levels placed at 5, 20, 50, 100, 250, 700, and 2000 meters are used. The upper levels are more closely spaced to provide better resolution in the near surface domain where the largest variation in dependent variables is found. Horizontally the grid points are spaced 3.0 degrees longitude and 2.5 degrees latitude. The horizontal and vertical domains are pictured in figures 2.1 and 2.2 respectively.

This model is similar to the primitive equation models of Haney (1971), Bryan (1969), and Bryan and Cox (1968) except for the introduction of salinity as an explicit dependent variable. The solution of the equations of motion involves the use of a streamfunction for the vertical mean motion. This somewhat artificial constraint allowed the use of a large time step and saved considerable computation time.

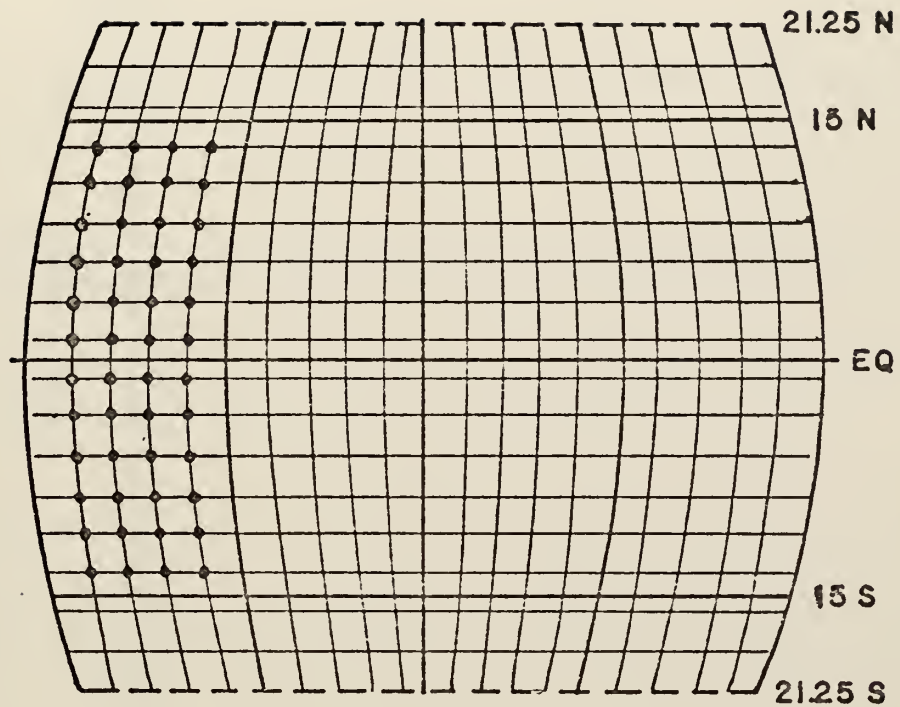


Figure 2.1 Horizontal domain of the model. Horizontal velocity components u and v were carried between grid points. The variables T , S , p , ψ , w were carried on the grid points. Grid spacing was 3.0 degrees longitude and 2.5 degrees latitude.

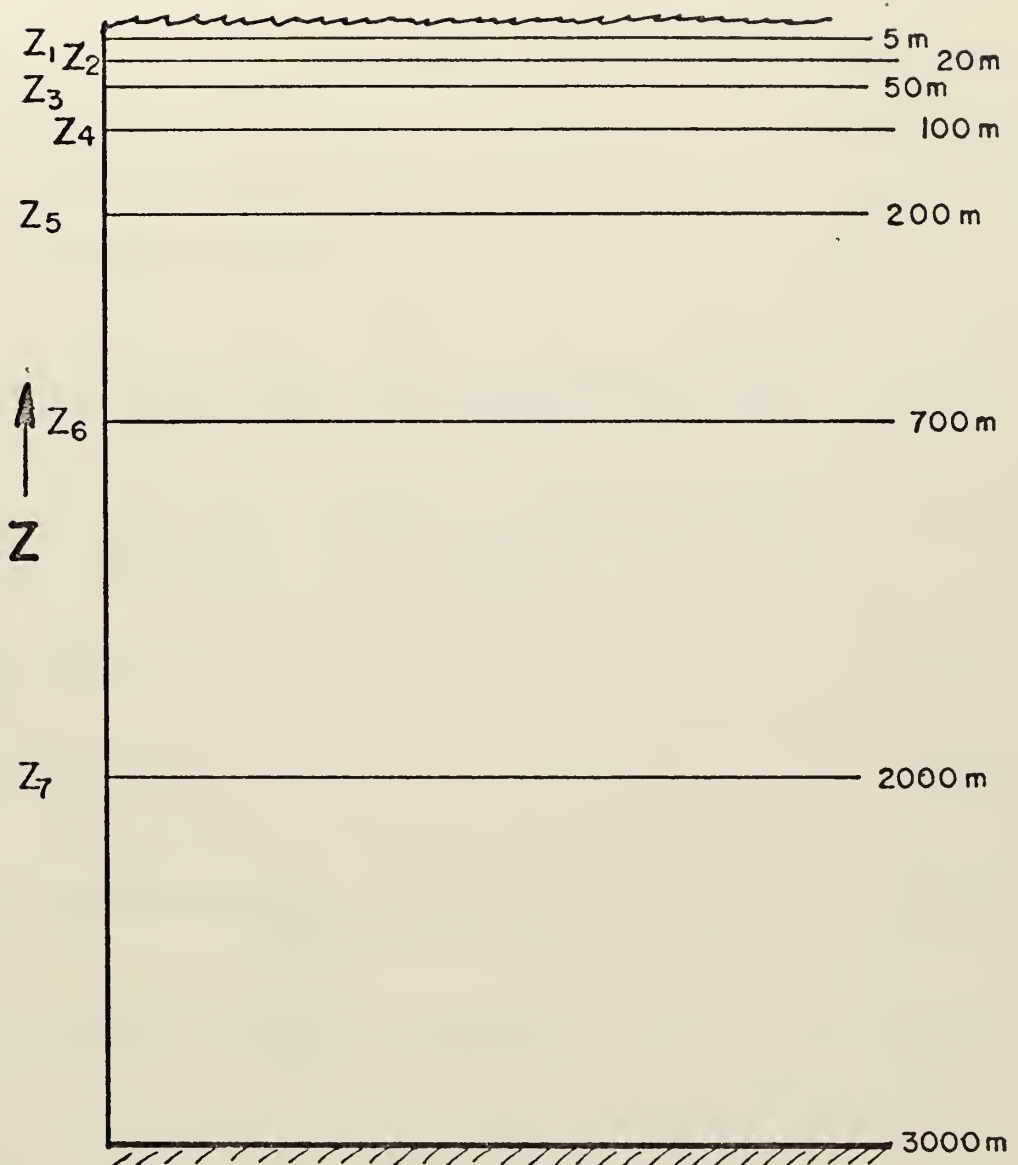


Figure 2.2 Vertical structure of the model showing seven levels with dense packing near the surface. All variables were stored at these levels except w ; the vertical velocity, which was found at intermediate levels (not shown, see figure 2.8).

The model is based upon the finite difference forms of the primitive equations which are integrated in time from a known set of initial conditions. The governing equations are the two horizontal equations of motion, the hydrostatic equation, the continuity equation, thermodynamic equation, the salinity equation, and the equation of state

$$\frac{du}{dt} = - \frac{1}{\rho_0 a \cos \varphi} \frac{dp}{d\lambda} + \left(2\Omega + \frac{u}{a \cos \varphi} \right) v \sin \varphi + F_\lambda, \quad (2.1)$$

$$\frac{dv}{dt} = - \frac{1}{\rho_0 a} \frac{dp}{d\varphi} - \left(2\Omega + \frac{u}{a \cos \varphi} \right) u \sin \varphi + F_\varphi, \quad (2.2)$$

$$\frac{dp}{dz} = - \rho g, \quad (2.3)$$

$$\nabla \cdot \mathbf{V} + \frac{dw}{dz} = 0, \quad (2.4)$$

$$\frac{dT}{dt} = A_H \nabla^2 T + k_H \frac{d^2 T}{dz^2} + C_T(T, S), \quad (2.5)$$

$$\frac{dS}{dt} = A_S \nabla^2 S + k_S \frac{d^2 S}{dz^2} + C_S(T, S), \quad (2.6)$$

$$\rho = \rho_0 [1 - \alpha(T - T_0) + \beta(S - S_0)], \quad (2.7)$$

where the symbols are as follows:

t time

λ longitude

φ latitude

z height

Ω angular speed of the earth

a	radius of the earth
g	acceleration of gravity
u	zonal current component
v	meridional current component
w	horizontal velocity
w	vertical speed
T	temperature
T_0	constant reference temperature
S	salinity
S_0	constant reference salinity
$C_T(T, S)$	rate of change of T due to instantaneous convective adjustment
$C_S(T, S)$	rate of change of S due to instantaneous convective adjustment
ρ	density
ρ_0	density of water at reference salinity S_0 and temperature T_0
α	coefficient of thermal expansion of sea water
B	coefficient of saline contraction of sea water
k_H, k_S	vertical eddy diffusion coefficients for heat and salt, respectively
A_H, A_S	lateral eddy diffusion coefficients for heat and salt, respectively
F_x	eastward frictional force per unit volume
F_y	northward frictional force per unit volume
∇	horizontal gradient operator.

The model circulation is determined primarily by the surface wind stress, and to a lesser extent by the fluxes of heat and salt at the surface. Figure 2.3 shows the annual latitudinal mean zonal stress for all oceans combined (Hellerman, 1967) which was used in this model. The distribution is practically symmetric except for the occurrence of a single minimum of the easterly stress north of the equator.

The net heat flux at the upper boundary is calculated according to Haney (1971) from the equation

$$Q = Q_1 + Q_2(T_A - T_1), \quad (2.8)$$

where:

Q is the net heat flux into the ocean,

Q_1 is that component of heat flux that would exist if there were no air-sea temperature difference (this is primarily radiative fluxes),

Q_2 is the contribution due to the existence of a temperature differential between the ocean and the atmosphere (this is primarily sensible and latent heat fluxes), and

T_A is a prescribed surface air temperature.

Haney's results, which were based on climatological data after London (1957), were averaged across the equator to obtain the symmetric patterns of Q_1 , Q_2 , and T_A shown in figure 2.4. This form of boundary condition essentially couples the ocean surface temperature to a prescribed

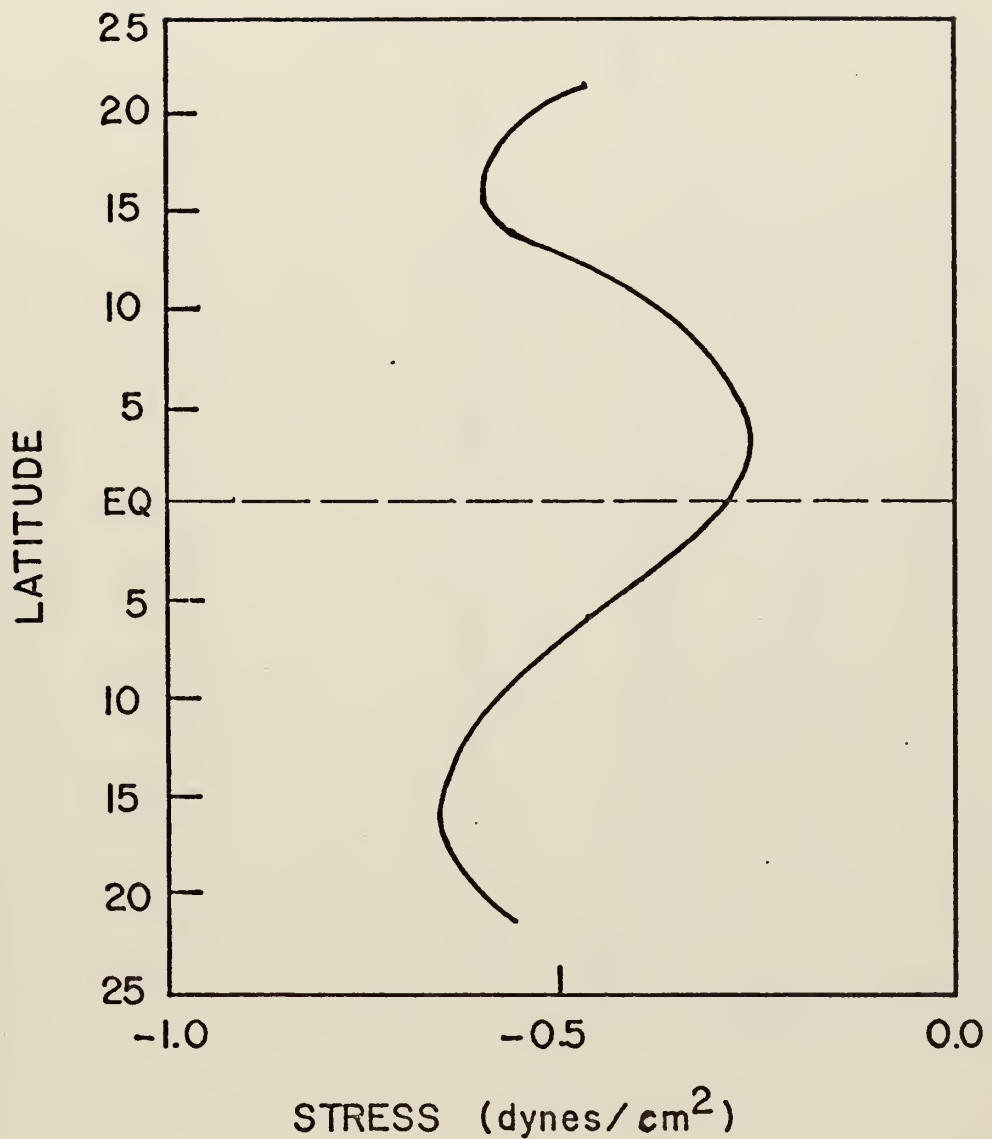


Figure 2.3 The annual latitudinal mean zonal stress for all oceans combined after Hellerman (1967).

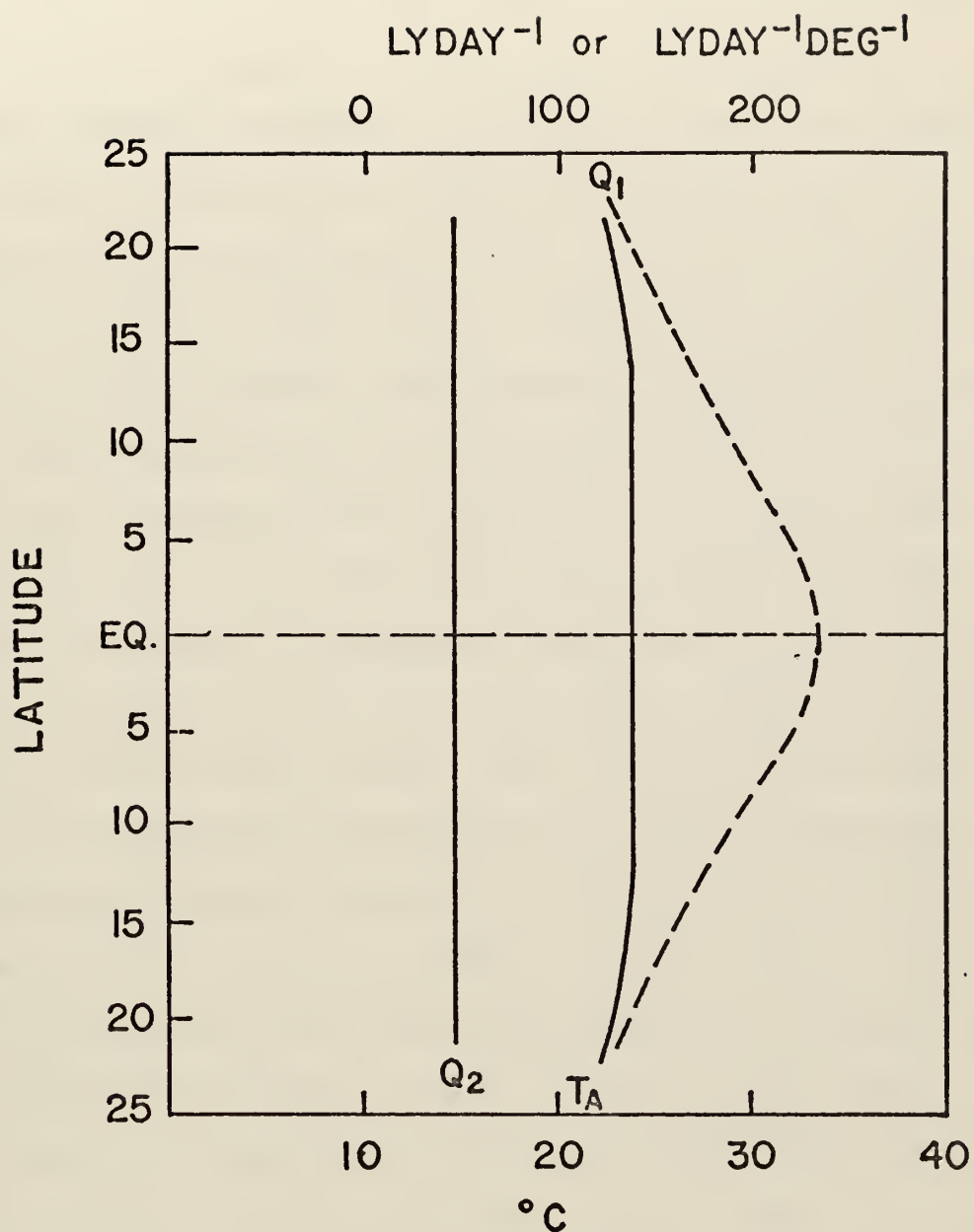


Figure 2.4 The atmospheric surface air temperature (bottom scale in degrees Celsius) and the heat flux components Q_1 and Q_2 in lyday^{-1} and $\text{lyday}^{-1}\text{deg}^{-1}$ (top scale).

atmospheric temperature. To accomplish a net heat flux of zero requires that T_A be less than T_1 over at least some portions of the domain.

The boundary condition on salinity is quite different from that on temperature because the downward flux of salinity is determined by the rate of removal of fresh water from the surface of the ocean. Rather than specifying the salinity at the surface, the downward flux of salt was specified from the zonal mean climatological rates of precipitation and evaporation after Budyko (1963). These curves are shown in figure 2.5. The data were averaged across the equator to obtain the symmetric curve shown by the dotted line. In this way, the only asymmetric boundary condition was the surface wind stress. This curve has the property that the meridionally integrated net rate of evaporation minus precipitation is zero and, since no flux of salt was allowed at the lateral boundaries or ocean floor, was sufficient to guarantee that the volume averaged salinity of the ocean remained constant in time. This does not imply, however, that no variations in surface salinity patterns would tend to occur. Clearly, near the equator where E-P has a local maximum, a local maximum of salt would tend to be formed. In the region of the model where precipitation exceeded evaporation the most, a local minimum would tend to be formed. Whether the horizontal and vertical gradients of salt caused by the upper boundary condition would modify the model circulation was an important question to be answered by this investigation.

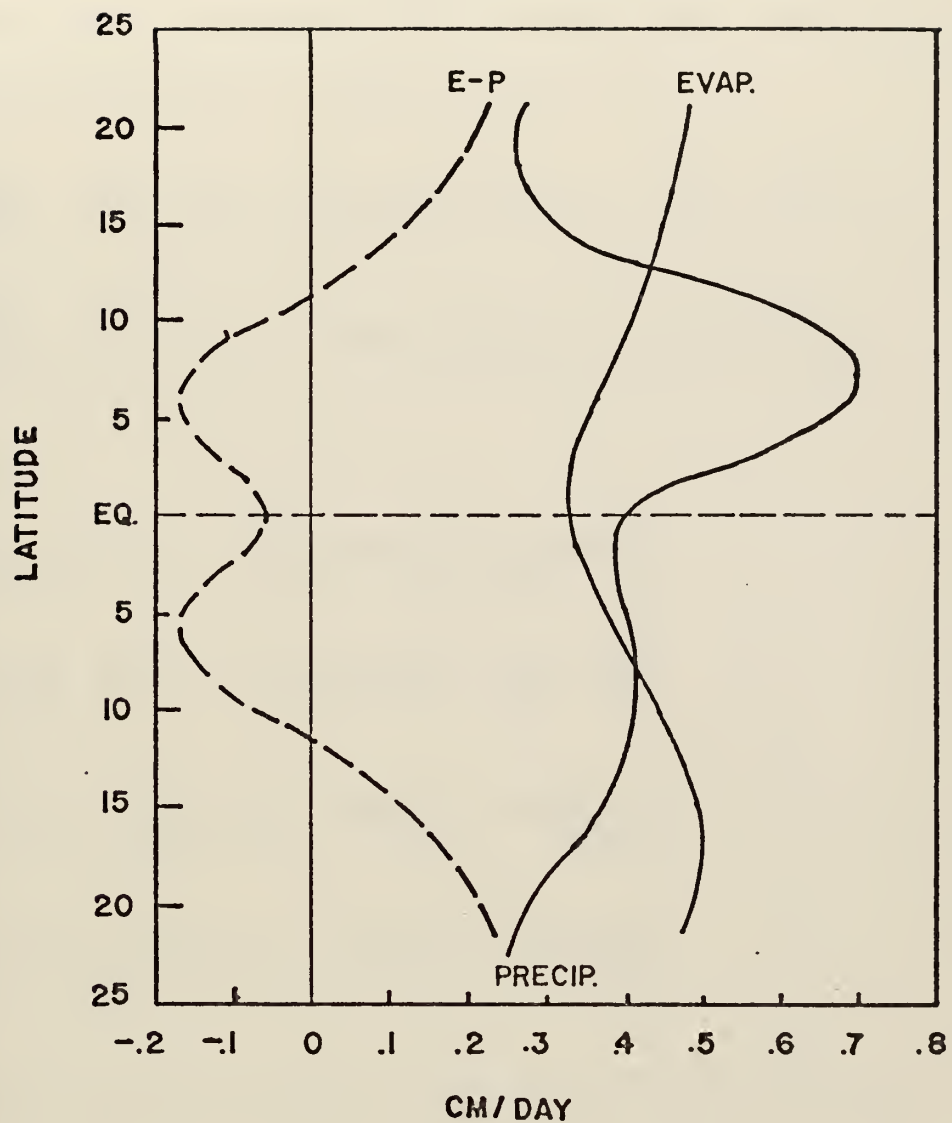


Figure 2.5 Evaporation and precipitation rates (solid lines) after Budyko (1963). The net rate of evaporation minus precipitation averaged across the equator is shown by the dashed line.

Details of the space differencing of the momentum equations are given by Haney (1971), and only the equations of temperature and salinity are treated here. These are conveniently written in symbolic form as

$$\frac{ds}{dt} = \text{SALT ADV.} + \text{SALT DIFFUSION} + \text{CONV. ADJ.}, \quad (2.9)$$

$$\frac{dT}{dt} = \text{TEMP ADV.} + \text{TEMP DIFFUSION} + \text{CONV. ADV.}, \quad (2.10)$$

where:

$$\text{SALT ADV.} = - \left[\nabla_2 \cdot (\nabla s) + \frac{\partial}{\partial z} (w s) \right], \quad (2.11)$$

$$\text{TEMP ADV.} = - \left[\nabla_2 \cdot (\nabla T) + \frac{\partial}{\partial z} (w T) \right], \quad (2.12)$$

$$\text{SALT DIFFUSION} = A_s \nabla^2 s + k_s \frac{\partial^2 s}{\partial z^2}, \quad (2.13)$$

$$\text{TEMP DIFFUSION} = A_h \nabla^2 T + k_h \frac{\partial^2 T}{\partial z^2}, \quad (2.14)$$

and A_s , k_s , A_h , and k_h are the diffusion coefficients as previously listed. Other numerical models have used values of $A_s \sim 10^8 \text{ cm}^2 \text{ sec}^{-1}$ and $k_s \sim 1 \text{ cm}^2 \text{ sec}^{-1}$ (Bryan, 1969; Munk, 1950). Because such a simple form of mixing was used, it was reasonable to use similar values for these coefficients. The coefficients of vertical eddy diffusion of heat and salt were $k_h, k_s = 1.0 \text{ cm}^2 \text{ sec}^{-1}$. The coefficients of horizontal eddy diffusion of heat and salt were $A_h, A_s = 2.5 \times 10^7 \text{ cm}^2 \text{ sec}^{-1}$. The friction terms in the equation of motion were

similarly formulated in terms of simple horizontal and vertical eddy diffusion of momentum with coefficients $A_M = 1.0 \times 10^8 \text{ cm}^2 \text{sec}^{-1}$ and $k_M = 10.0 \text{ cm}^2 \text{sec}^{-1}$. This gave a ratio of k_M to k_H of ten which appeared to give good results; Krivelevich (1970) found a ratio of twenty to give the best results in a forty layer, two-dimensional equatorial model.

The discussion of the "CONVECTIVE ADJUSTMENT" is given in a later section, and only the differencing of the advection and diffusion terms are treated here. Furthermore, since the forms of equations (2.9) and (2.10) are identical, and both variables S and T are located at the same grid points, only the finite differencing of the salinity equation is given. However, because the surface boundary conditions are different for the vertical diffusion terms of each, a separate treatment of them is necessary. Although all finite differencing was done in curvilinear coordinates, only the cartesian forms are shown for the purposes of demonstrating the techniques involved.

B. HORIZONTAL AND VERTICAL FINITE DIFFERENCING

1. The Horizontal Grid

A portion of the horizontal grid of size 21×18 is shown in figure 2.6. The temperature T and salinity S are located at the i and j grid points, whereas the velocity components u and v are located at intermediate points; Δx is the E-W grid distance, and Δy the N-S grid distance.

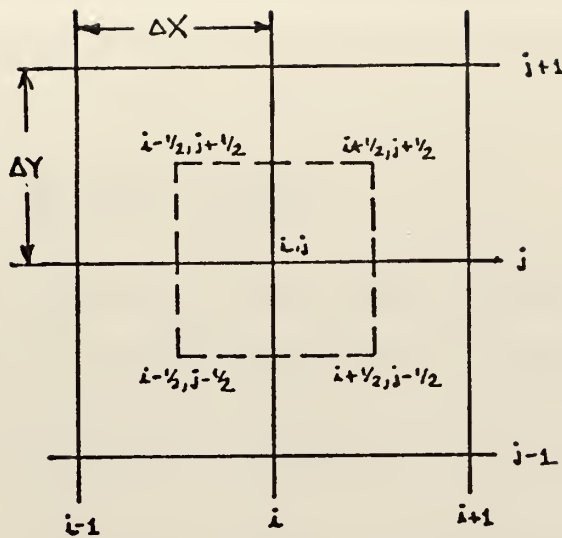


Figure 2.6 The horizontal space staggered grid with salinity S and temperature T located at the i and j grid points and the velocity components u and v at intermediate points; ΔX is the E-W grid distance and ΔY the N-S grid distance.

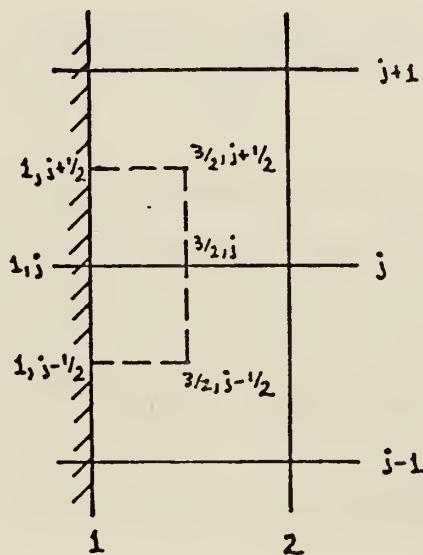


Figure 2.7 Grid points near the western wall used to derive the finite difference analogues along the boundary at the general grid point $(1, j)$.

2. Differencing of Horizontal Advection

Expanding the horizontal advection portion of equation (2.11) gives

$$\nabla \cdot (\mathbf{v} S) = \frac{\partial (uS)}{\partial x} + \frac{\partial (vS)}{\partial y}. \quad (2.15)$$

Considering first only those grid points interior to the boundaries and using centered finite differencing at the general grid point (i, j) gives

$$\nabla \cdot (\mathbf{v} S)_{i,j} = \frac{(uS)_{i+\frac{1}{2},j} - (uS)_{i-\frac{1}{2},j}}{\Delta x} + \frac{(vS)_{i,j+\frac{1}{2}} - (vS)_{i,j-\frac{1}{2}}}{\Delta y} \quad (2.16)$$

Since neither u or v is explicitly defined at the half integer points, a linear approximation is used; for example, the term $(uS)_{i+\frac{1}{2},j}$ is approximated as

$$(uS)_{i+\frac{1}{2},j} = \left[\frac{u_{i+\frac{1}{2},j+\frac{1}{2}} + u_{i+\frac{1}{2},j-\frac{1}{2}}}{2} \right] \left[\frac{S_{i+1,j} + S_{i,j}}{2} \right] \quad (2.17)$$

Using a similar procedure for the remaining three terms in equation (2.16) gives the final differenced form for equation (2.15),

$$\begin{aligned} \nabla \cdot (\mathbf{v} S)_{i,j} = & \left[u_{i+\frac{1}{2},j+\frac{1}{2}} + u_{i+\frac{1}{2},j-\frac{1}{2}} \right] \left[S_{i+1,j} + S_{i,j} \right] / (4\Delta x) \\ & - \left[u_{i-\frac{1}{2},j+\frac{1}{2}} + u_{i-\frac{1}{2},j-\frac{1}{2}} \right] \left[S_{i-1,j} + S_{i,j} \right] / (4\Delta x) \\ & + \left[v_{i-\frac{1}{2},j+\frac{1}{2}} + v_{i+\frac{1}{2},j+\frac{1}{2}} \right] \left[S_{i,j+1} + S_{i,j} \right] / (4\Delta y) \\ & - \left[v_{i-\frac{1}{2},j-\frac{1}{2}} + v_{i+\frac{1}{2},j-\frac{1}{2}} \right] \left[S_{i,j-1} + S_{i,j} \right] / (4\Delta y). \end{aligned} \quad (2.18)$$

The use of a centered difference for points along the boundaries is not practical because the velocity components u and v are not specified exterior to the walls. The finite difference analogues are derived by specifying boundary conditions and using one-sided approximations to the derivative when necessary. Because the mathematical forms of the difference analogues are similar for all four walls, it is sufficient to demonstrate the differencing for only one of them. A segment of the western boundary region, as pictured in figure 2.7, is used to derive the difference approximation at the general point $(1,j)$.

Since the normal component of the current u must vanish along the western wall, the first term of equation (2.15) reduces to

$$\frac{d}{dx} (uS)_{1,j} = \frac{(uS)_{3/2,j} - (uS)_{1,j}}{\frac{\Delta x}{2}} \quad (2.19)$$

Further reduction leads to

$$\frac{d}{dx} (uS)_{1,j} = \frac{(u\nu_{1,j-\frac{1}{2}} + u\nu_{1,j+\frac{1}{2}})(S_{1,j} + S_{2,j})}{2\Delta x} \quad (2.20)$$

To derive the second term of equation (2.15), it is assumed that free slip applies for the meridional speed component v , that is,

$$v_{1,j-\frac{1}{2}} = v_{1/2,j-\frac{1}{2}}, \text{ and} \quad (2.21)$$

$$v_{1,j+\frac{1}{2}} = v_{3/2,j+\frac{1}{2}} \quad . \quad (2.22)$$

In finite difference form the term is

$$\frac{\partial}{\partial y} (vS)_{1,j} = \frac{(vS)_{1,j+\gamma_2} - (vS)_{1,j-\gamma_2}}{\Delta y} . \quad (2.23)$$

Application of the boundary conditions given by equations (2.21) and (2.22) gives

$$\frac{\partial}{\partial y} (vS)_{1,j} = \frac{(v_{3/2,j+\gamma_2})(S_{1,j} + S_{1,j+1}) - (v_{3/2,j-\gamma_2})(S_{1,j-1} + S_{1,j})}{2\Delta y} . \quad (2.24)$$

3. Differencing of Horizontal Diffusion

Expansion of the horizontal diffusion portion of equation (2.13) gives

$$As \nabla^2 S = As \left[\frac{d^2 S}{dx^2} + \frac{d^2 S}{dy^2} \right] . \quad (2.25)$$

This is rewritten as

$$As \nabla^2 S = As \left[\frac{d}{dx} \left(\frac{dS}{dx} \right) + \frac{d}{dy} \left(\frac{dS}{dy} \right) \right] . \quad (2.26)$$

Evaluation at the general interior grid point (i,j) results in the equation

$$As \nabla^2 S_{1,j} = \frac{As \left[\frac{dS}{dx} \right]_{i+\gamma_2,j} - \left[\frac{dS}{dx} \right]_{i-\gamma_2,j}}{\Delta x} + \frac{As \left[\frac{dS}{dy} \right]_{i,j+\gamma_2} - \left[\frac{dS}{dy} \right]_{i,j-\gamma_2}}{\Delta y} . \quad (2.27)$$

Application of a centered derivative to each first order term gives the final result,

$$\begin{aligned} As \nabla^2 S_{i,j} &= \frac{As [S_{i-1,j} - 2S_{i,j} + S_{i+1,j}]}{(\Delta x)^2} \\ &+ \frac{As [S_{i,j-1} - 2S_{i,j} + S_{i,j+1}]}{(\Delta y)^2} . \end{aligned} \quad (2.28)$$

The differencing of equation (2.25) along the ocean walls is handled similar to the evaluation of the horizontal advection terms along the boundaries; the differencing will be illustrated for an arbitrary point $(1,j)$ along the western boundary. Boundary conditions along the wall are those of perfect insulation,

$$\frac{ds}{dx} \Big|_{i,j} = 0 . \quad (2.29)$$

Writing equation (2.25) in finite difference form at point $(1,j)$ gives

$$As \nabla^2 S_{1,j} = \frac{As \left[\frac{ds}{dx} \Big|_{1/2,j} - \frac{ds}{dx} \Big|_{1,j} \right]}{\frac{\Delta x}{2}} + \frac{As \left[\frac{ds}{dy} \Big|_{1,j+1/2} - \frac{ds}{dy} \Big|_{1,j-1/2} \right]}{\Delta y} . \quad (2.30)$$

Application of the boundary conditions and further reduction of the first order terms gives the final result,

$$As \nabla^2 S_{1,j} = 2As \left[\frac{S_{2,j} - S_{1,j}}{(\Delta x)^2} \right] + As \left[\frac{S_{1,j+1} - 2S_{1,j} + S_{1,j-1}}{(\Delta y)^2} \right] . \quad (2.31)$$

4. The Vertical Grid

Figure 2.8 shows the placement of layers in the vertical. The vertical index k and all of the variables (u, v, S, T, p) are defined at the integer levels shown by the solid lines, whereas w is defined at the half integer levels indicated by dotted lines. The $(KM + 1)$ unequal thicknesses are defined as

$$\Delta z_{k-1/2} = z_{k-1} - z_k, \quad k=2 \dots KM, \quad (2.32)$$

$$\Delta z_{1/2} = -2z_1, \quad (2.33)$$

$$\Delta z_{KM+1/2} = 2(z_{KM} + H), \quad (2.34)$$

where $z_k < 0$ while $H > 0$ is the ocean depth. This definition satisfies the equation

$$\frac{1}{2} [\Delta z_{1/2}] + \sum_{k=2}^{KM} \Delta z_{k-1/2} + \frac{1}{2} [\Delta z_{KM+1/2}] = H. \quad (2.35)$$

The thicknesses centered at the levels at which (u, v, S, T, p) are located are defined as the average of the two adjacent half integer levels, that is,

$$\Delta z_k = \frac{1}{2} [\Delta z_{k-1/2} + \Delta z_{k+1/2}], \quad k=1, KM. \quad (2.36)$$

This definition has the property that

$$\sum_{k=1}^{KM} \Delta z_k = H. \quad (2.37)$$

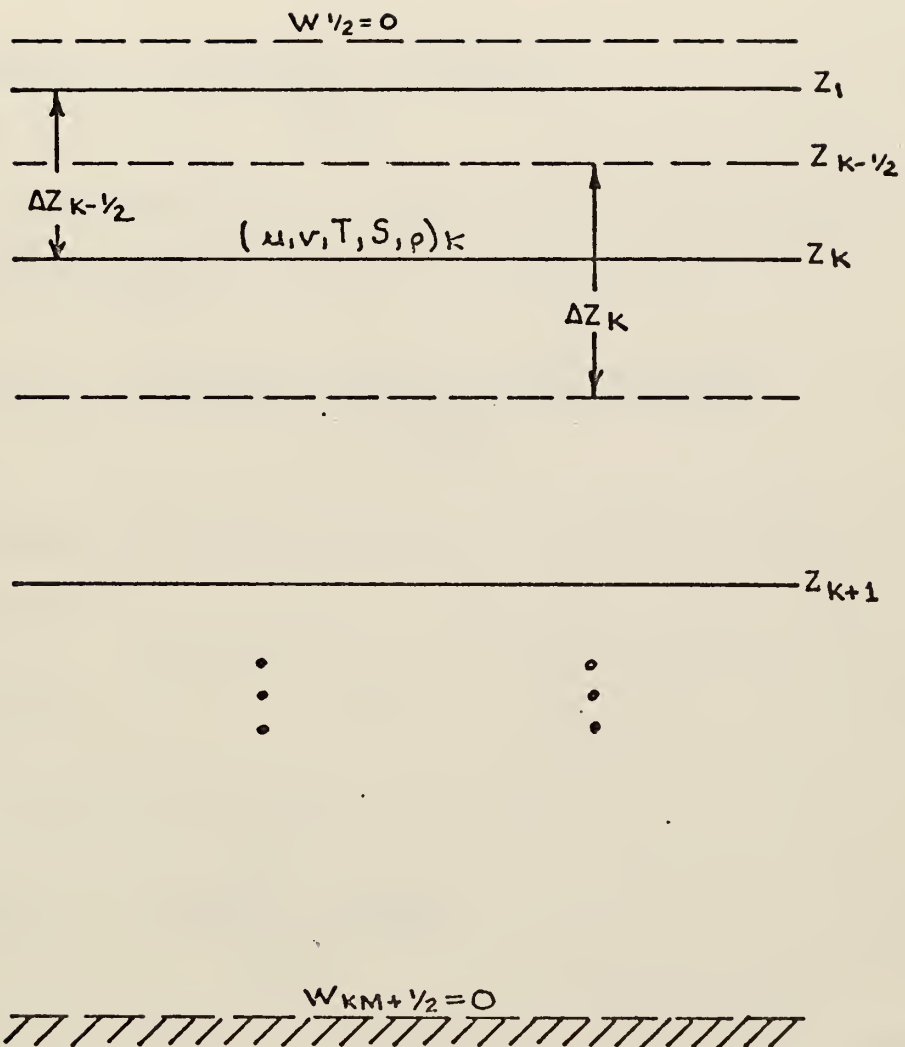


Figure 2.8 Location of the variables in the vertical grid.

5. Finite Differencing of Vertical Advection

Considering the intermediate levels $\Delta z_2, \dots, \Delta z_{K-1}$, the vertical advection portion of equation (2.11) is written at the K^{th} level as

$$\frac{\partial}{\partial z} (wS)_K = \frac{(wS)_{K-1/2} - (wS)_{K+1/2}}{\Delta z_K}. \quad (2.38)$$

Since S is not available at half levels, the average of the salinities at adjacent levels is used to give

$$\frac{\partial}{\partial z} (wS)_K = \frac{w_{K-1/2} (S_{K-1} + S_K) - w_{K+1/2} (S_K + S_{K+1})}{2 \Delta z_K}. \quad (2.39)$$

At the upper boundary the vertical velocity is zero, mathematically

$$w_{1/2} = 0. \quad (2.40)$$

Equation (2.38) evaluated at $K=1$ gives

$$\frac{\partial}{\partial z} (wS)_1 = \frac{(wS)_{1/2}^{\circ} - (wS)_{3/2}}{\Delta z_1}. \quad (2.41)$$

Further expansion gives the analogue at the level nearest the surface as

$$\frac{\partial}{\partial z} (wS)_1 = \frac{-w_{1/2} (S_1 + S_2)}{2 \Delta z_1}. \quad (2.42)$$

At the ocean floor $w_{KM+1/2} = 0$, and at the bottom level equation (2.38) becomes

$$\frac{\partial}{\partial z} (wS)_{KM} = \frac{w_{KM-1/2} (S_{KM-1} + S_{KM})}{2 \Delta z_{KM}}. \quad (2.43)$$

6. Differencing of Vertical Diffusion

Considering the interior levels first, the vertical diffusion portion of equation (2.13) is written at the general k th level as

$$k_s \frac{d^2 S}{dz^2} \Big|_k = \frac{k_s \left[\frac{dS}{dz} \Big|_{k-1/2} - \frac{dS}{dz} \Big|_{k+1/2} \right]}{\Delta z_k}. \quad (2.44)$$

Further reduction of the first order derivative terms gives

$$k_s \frac{d^2 S}{dz^2} \Big|_k = \frac{k_s \left[\frac{S_{k-1} - S_k}{\Delta z_{k-1/2}} - \frac{S_k - S_{k+1}}{\Delta z_{k+1/2}} \right]}{\Delta z_k}, \quad k=2 \dots KM-1 \quad (2.45)$$

The lower boundary condition of perfect insulation at $z = -H$ and index $KM+1/2$ is

$$\frac{dS}{dz} \Big|_{KM+1/2} = 0. \quad (2.46)$$

Using this boundary condition gives

$$k_s \frac{d^2 S}{dz^2} \Big|_{KM} = \frac{k_s \left[\frac{dS}{dz} \Big|_{KM-1/2} - \frac{dS}{dz} \Big|_{KM+1/2} \right]}{\Delta z_{KM}}, \quad (2.47)$$

and the analogue for the lowest level becomes

$$k_s \frac{d^2 S}{dz^2} \Big|_{K=1} = \frac{k_s [S_{K=1} - S_{K=2}]}{\Delta z_{K=1} \cdot \Delta z_{K=1} - \gamma_2}. \quad (2.48)$$

Up to this point the finite differencing of the salinity and temperature equations has required only a single treatment as both equations have similar mathematical forms and boundary conditions. The difference analogue for a term in the heat equation is obtained from its counterpart in the salinity equation by replacing S with the variable T . At the ocean surface this procedure does not apply since the boundary conditions are very different.

The upper boundary condition for the heat equation is

$$k_T \frac{dT}{dz} \Big|_{K=1} = \frac{Q}{\rho_0 C} \quad (2.49)$$

where $Q = Q_1 + Q_2(T_A - T_1)$. Equation (2.8) is a relatively strong condition that ties T_1 , the temperature at the first level below the surface, rather closely to the specified atmospheric temperature T_A . Should some mechanism cause a large difference between the two, heat fluxes are created that tend to restore the difference to a small value.

The boundary condition for salt on the other hand is

$$k_s \frac{dS}{dz} \Big|_{K=1} = S_1(E - P). \quad (2.50)$$

This is a relatively weak condition of nearly constant flux which tended to make the model ocean respond very slowly to the surface salt flux. Areas where the rate of evaporation exceeded that of precipitation tended to get more salty until advection and/or diffusion became sufficient to create a balanced state. Similarly, areas with excess precipitation tended to become less salty with the approach toward steady state being very slow. The reasons for the slow salinity relaxation time and its effects upon the dynamics of the model are thoroughly discussed in Section III.

The finite difference form of the vertical diffusion term in the salinity equation at level $k=1$ is

$$k_s \frac{d^2s}{dz^2} \Big|_1 = \frac{k_s \left[\frac{ds}{dz} \Big|_{z_2} - \frac{ds}{dz} \Big|_{z_1/2} \right]}{\Delta z_1}. \quad (2.51)$$

Use of the boundary condition (equation 2.50) gives

$$k_s \frac{d^2s}{dz^2} \Big|_1 = \frac{\left[S_1(E-P) - k_s \frac{ds}{dz} \Big|_{z_2} \right]}{\Delta z_1}, \quad (2.52)$$

which reduces to the final form

$$k_s \frac{d^2s}{dz^2} \Big|_1 = \left[\frac{S_1(E-P)}{\Delta z_1} - \frac{k_s (S_1 - S_2)}{\Delta z_1 \cdot \Delta z_{1/2}} \right]. \quad (2.53)$$

In a similar manner the difference form of the vertical diffusion term in the heat equation at the level

$k=1$ is

$$k_T \frac{d^2T}{dz^2} \Big|_1 = \frac{k_T \left[\frac{dT}{dz} \Big|_{z_2} - \frac{dT}{dz} \Big|_{z_1} \right]}{\Delta z_1}. \quad (2.54)$$

Using the upper boundary condition for heat (equation 2.49) yields

$$k_T \frac{d^2T}{dz^2} \Big|_1 = \left[\frac{Q_1 + Q_2 (T_A - T_1)}{\rho_0 C \Delta z_1} - \frac{k_T (T_1 - T_2)}{\Delta z_1 \Delta z_2} \right]. \quad (2.55)$$

C. EQUATION OF STATE

1. Density as a Function of Temperature and Salinity

Density depends in a nonlinear fashion upon temperature, salinity, and pressure; however, the assumption of incompressibility reduces the dependence to two variables, salinity and temperature. If ρ_0 is the density corresponding to arbitrary reference values of temperature T_0 and salinity S_0 , it follows from a Taylor series expansion about T_0 and S_0 that the new value of density at salinity $S_0 + \Delta S$ and $T_0 + \Delta T$ is given by

$$\rho(S_0 + \Delta S, T_0 + \Delta T) = \rho(S_0, T_0) + \frac{d\rho}{dS} \Delta S + \frac{d\rho}{dT} \Delta T + \dots \frac{1}{n!} \left[\Delta S \frac{d}{dS} + \Delta T \frac{d}{dT} \right]^n \rho_0 \dots \quad (2.56)$$

Data taken from Von Arx (1964) and reproduced as figure 2.9 shows that over the range of salinities and densities commonly found in equatorial oceans, the nonlinear terms may be dropped with little sacrifice in accuracy and

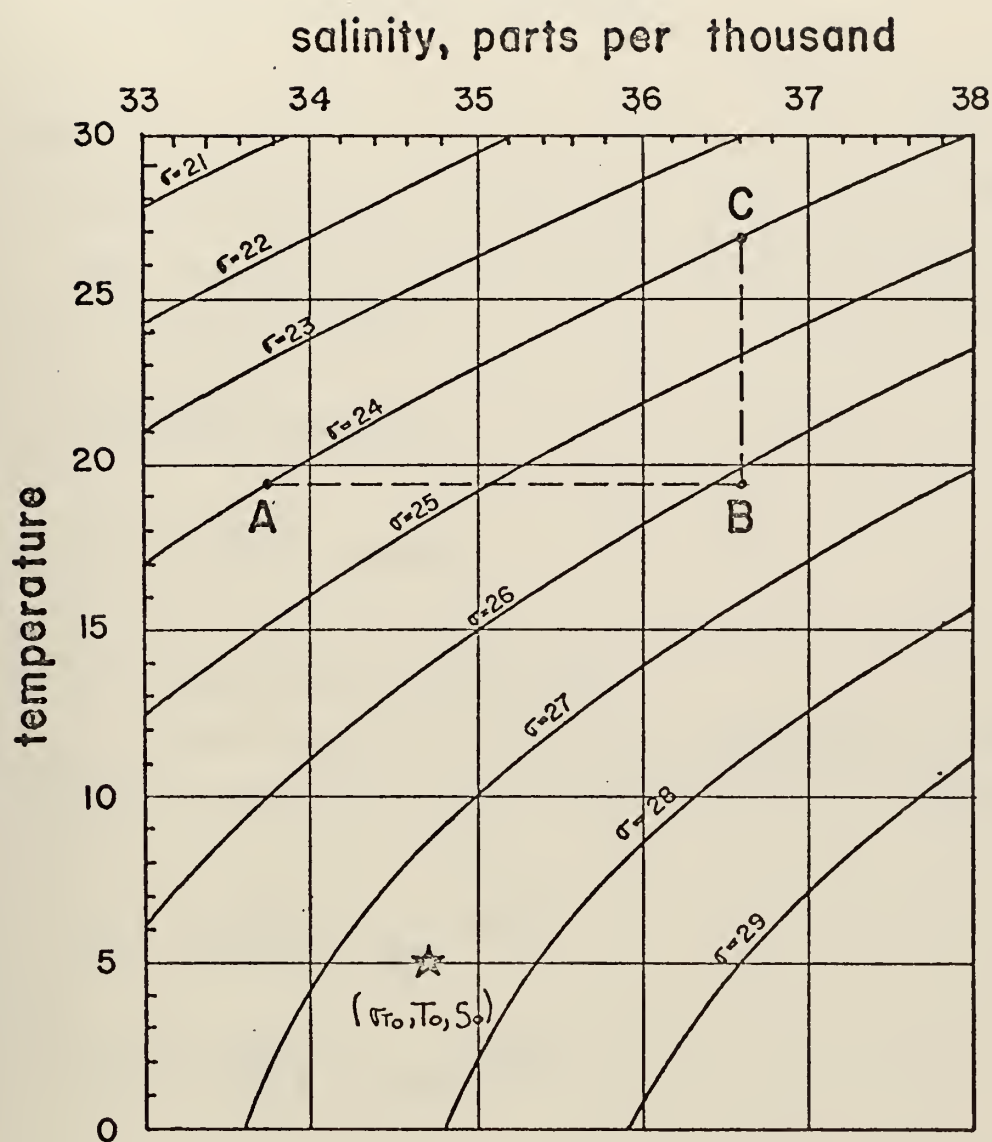


Figure 2.9 Plot of sigma-t vs. temperature and salinity after Von Arx (1964).

the equation written as

$$\rho = \rho_0 [1 - \alpha(T - T_0) + \beta(S - S_0)], \quad (2.57)$$

where

ρ = the density at temperature T and salinity S ,

ρ_0 = the density at reference temperature T_0 and salinity S_0 ,

$$\alpha = -\frac{1}{\rho_0} \frac{d\rho}{dT} \Big|_{S=\text{CONST.}}, \quad (2.58)$$

$$\beta = \frac{1}{\rho_0} \frac{d\rho}{dS} \Big|_{T=\text{CONST.}} \quad (2.59)$$

2. Solutions for α and β

Introducing the quantity $\Gamma_T = (\rho_{S,T,0} - 1) \times 10^3$

where the subscript zero refers to sea level pressure, gives

$$\alpha = \frac{1}{\rho_0} \frac{d\Gamma_T}{dT} \Big|_{S=\text{CONST}} \times 10^3, \quad (2.60)$$

$$\beta = \frac{1}{\rho_0} \frac{d\Gamma_T}{dS} \Big|_{T=\text{CONST}} \times 10^{-3}. \quad (2.61)$$

Both α and β are determined from figure 2.9 by graphically taking a finite difference approximation to equations (2.60) and (2.61) to give

$$\alpha = -\frac{1}{\rho_0} \frac{d\Gamma_T}{dT} \Big|_{S=\text{CONST}} \times 10^{-3} \sim -\frac{1}{\rho_0} \frac{(\Gamma_{C} - \Gamma_{B})}{(T_C - T_B)} \times 10^{-3} = 2.75 \times 10^{-4} \text{ deg}^{-1}, \quad (2.62)$$

$$\beta = \frac{1}{\rho_0} \frac{\partial \sigma}{\partial S} \Big|_{T \cdot \text{CONST}} \times 10^{-3} \sim \frac{1}{\rho_0} \frac{(\sigma_B - \sigma_A)}{(T_B - T_A)} \times 10^{-3} = 7.5 \times 10^{-4} (\sigma_{\text{ss}})^{-1} \quad (2.63)$$

The reference values ρ_0 , T_0 , and S_0 are 1.0276 gm-cm⁻³, 278.2°K, and 34.72‰ respectively; this reference state is marked by a star on figure 2.9. The approximations for α and β are taken, however, at a location on the T,S diagram which is representative of the temperature and salinity found near the surface in equatorial oceans and the dependence of density on these variables is nearly linear.

D. INSTANTANEOUS CONVECTIVE ADJUSTMENT OF DENSITY

Whenever a heavier water mass lies above one of lesser density, an unstable situation exists and natural buoyancy forces cause vertical mixing and a return to a neutral state. Since from the equation of state, density is a function of temperature and salinity, any mechanism that causes temperature to increase or salinity to decrease with depth is a potential source of instability. In this model the only heat flux into the ocean occurs at the surface. In a steady state, the surface averaged heat flux must be zero. Thus there are some regions where the net heat flux at the surface is downward and some regions where it is upward, and it is in these regions of upward heat flux that thermally-induced instability is found. Salinity-induced instability

occurs in regions of the model where evaporation exceeds precipitation causing a layer of heavy, salty water to exist near the surface. The vertical juxtaposition due to advection of water masses of equal temperature but different salt content is also a potential source of salinity-induced instability.

Instability in the real ocean lasts only a short period of time. Buoyancy forces produce large vertical velocities which mix the unstable layers very rapidly and efficiently, and quickly establish a uniform vertical distribution of mixed quantities. The following is a reasonable method of modeling this phenomena.

Figure 2.10 shows a vertical section of the ocean where the density increases with depth and represents the stable case where no convective instability will exist. Using previously introduced notation, several levels $k-1$, k , and $k+1$ and the vertical thickness Δz_k are shown. The intermediate levels $k-3/2$, $k-1/2$, $k+1/2$ and $k+3/2$ are shown as dashed lines and thicknesses corresponding to $k-1/2$ and $k+1/2$ are denoted as $\Delta z_{k-1/2}$ and $\Delta z_{k+1/2}$ respectively. Although in the real ocean the profile can be nonlinear, a linear profile as denoted by the solid lines in figure 2.11 is assumed in the model; this first order approximation is consistent with others used elsewhere and is sufficient to guarantee conservation of the quadratic quantity in the vertical advection terms. Additionally, it is assumed that

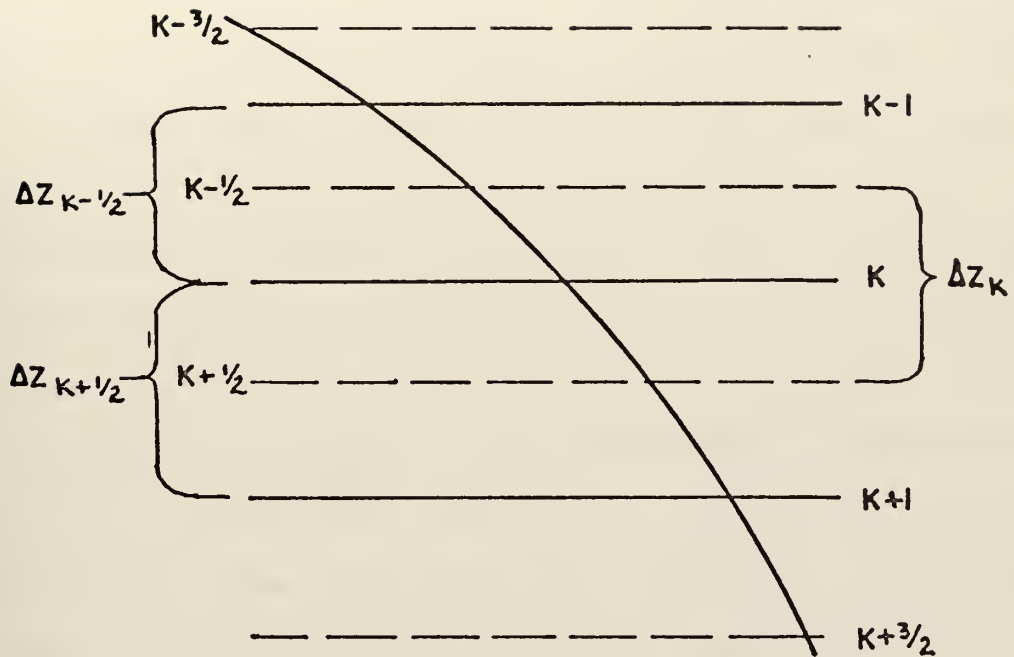


Figure 2.10 Stable Density Profile

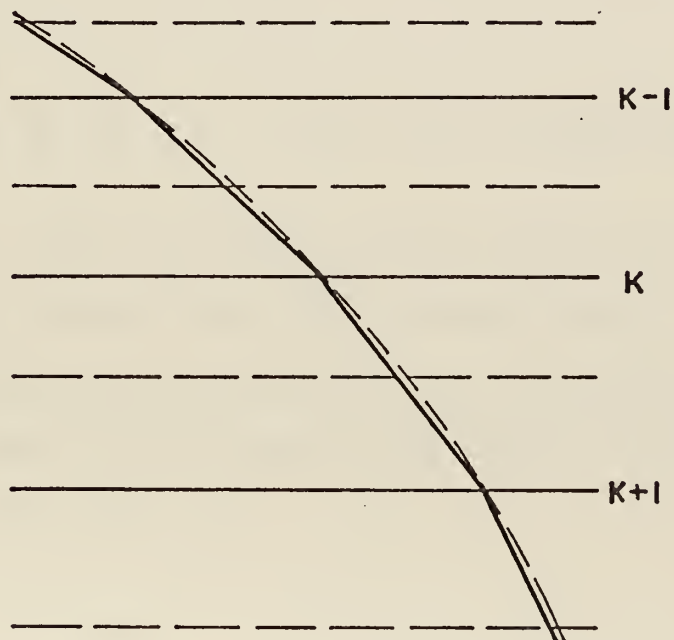


Figure 2.11 Model Equivalent of the Stable Density Profile

the density which is stored at each level represents the vertically integrated average of the entire Δz layer.

If $\rho_{k-1} > \rho_k$ for any two consecutive levels, then convective instability on a scale which is too small to be resolved by the grid will occur. Since from equation (2.57) density is a function of both salinity and temperature, either one or both may be the cause of the instability.

Figure 2.12 shows the case where density instability is due to temperature; salinity is assumed to be constant with depth. T_{k-1} represents the temperature for the upper layer of thickness Δz_{k-1} and T_k the temperature for the lower layer of thickness Δz_k . To insure stability, new temperatures T_{k-1}^* and T_k^* are determined such that a slightly stable temperature lapse rate results. Mathematically the following must hold:

$$\frac{T_{k-1}^* - T_k^*}{\Delta z_{k-1}} = \epsilon_T \quad \text{or} \quad T_{k-1}^* = T_k^* + \epsilon_T \Delta z_{k-1} \quad (2.64)$$

where ϵ_T is a small positive constant whose value is the new lapse rate shown as the short dotted line in figure 2.12. To insure conservation of heat, the thickness weighted average of the temperatures before and after mixing must be the same, that is,

$$T_{k-1} \Delta z_{k-1} + T_k \Delta z_k = T_{k-1}^* \Delta z_{k-1} + T_k^* \Delta z_k. \quad (2.65)$$

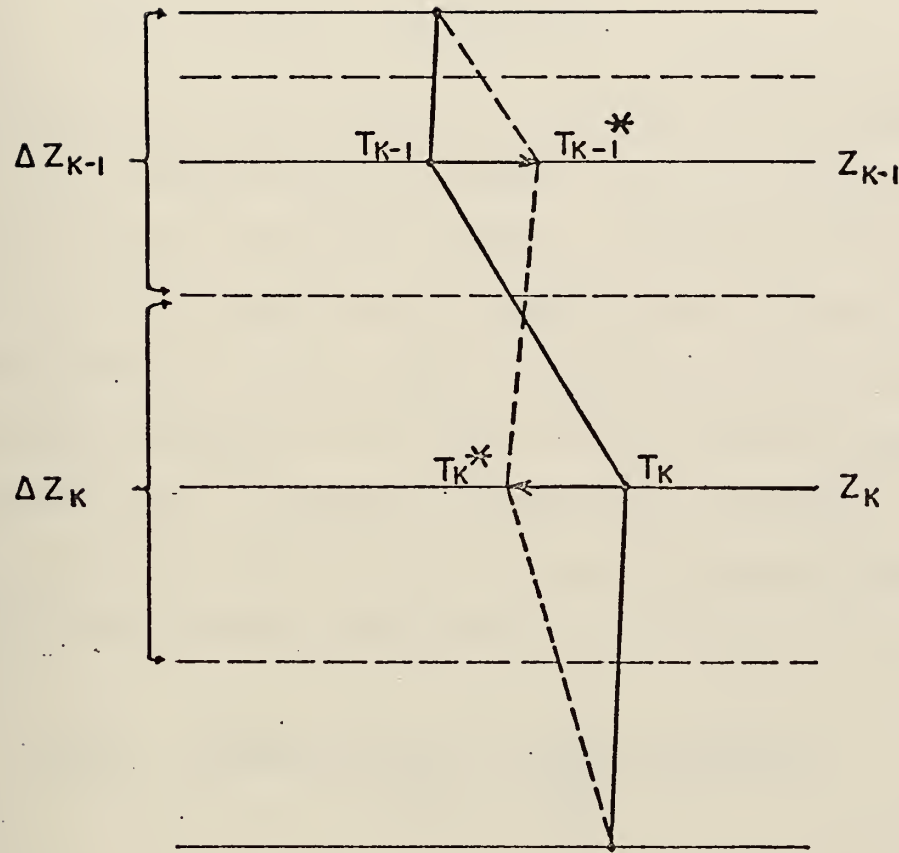


Figure 2.12 Diagram of an unstable state due to the temperature profile showing the necessary temperature adjustments to achieve stability between levels z_{k-1} and z_k . The solid line is before adjustment, the dashed is after.

Equations (2.64) and (2.65) comprise a set of two simultaneous equations in two unknowns and when solved give

$$T_k^* = \frac{T_k \Delta z_k + (T_{k-1} - \epsilon_T \Delta z_{k-1/2}) \Delta z_{k-1}}{\Delta z_{k-1} + \Delta z_k}, \quad (2.66)$$

$$T_{k-1}^* = T_k^* + \epsilon_T \Delta z_{k-1/2}. \quad (2.67)$$

Equations (2.66) and (2.67) define the new temperature values. If the temperature is constant but a decrease in salinity with depth causes instability, convective adjustment must take place such that the salinity values S_k and S_{k-1} are replaced by new ones S_k^* and S_{k-1}^* such that a stable, slightly positive vertical salinity gradient, ϵ_s , is established. Assuming conservation of salinity, and using a reasoning similar to that used for temperature, gives the following results analogous to (2.66) and (2.67):

$$S_k^* = \frac{S_k \Delta z_k + (S_{k-1} + \epsilon_s \Delta z_{k-1/2}) \Delta z_{k-1}}{\Delta z_{k-1} + \Delta z_k}, \quad (2.68)$$

$$S_{k-1}^* = S_k - \epsilon_s \Delta z_{k-1/2}. \quad (2.69)$$

For an incompressible ocean, the value for ϵ_T is zero, but it is reasonable to define it to be some small positive value to avoid possible instability due to round off error in the computation; ϵ_T is defined in terms of T_0 , the surface reference temperature, and H , the depth of the model ocean, as

$$\epsilon_T = \frac{10^{-4} T_0}{H}. \quad (2.70)$$

Having fixed ϵ_T , the appropriate value for ϵ_s and ϵ_p can be derived from the equation of state and the definitions of ϵ_s (2.64) and ϵ_T (2.70). If it is assumed that the salinity and temperature have equal weights in determining the density lapse rate, then it can be shown from the equation of state that

$$\epsilon_s = \frac{\alpha}{\beta} \epsilon_T, \quad (2.71)$$

$$\epsilon_p = 2\alpha \epsilon_T. \quad (2.72)$$

A very brief explanation of how the convective adjustment is programmed is as follows:

- (1) The density lapse rate, $((\rho_{k-1} - \rho_k) / \Delta z_{k-1, k})$, is computed for a layer and compared with the stable value ϵ_p .
- (2) If the density lapse rate is more stable than ϵ_p , no change is made in temperature or salinity; if it is less stable than ϵ_p , the temperature and salinity are both adjusted using equations (2.66), (2.67), (2.68), and (2.69).
- (3) All layers are processed in order from the first below the surface to the last above the lower boundary. In the convective adjustment of a pair of levels, it is possible to render an adjacent pair of levels unstable; therefore, the adjustment proceeds in repeated scans until no

adjustment of temperature or salinity is performed during a scan (see figure 2.12). The convective adjustment is then terminated.

III. RESULTS

A. THE TIME DEPENDENT BEHAVIOR OF THE MODEL

1. Salinity Relaxation Time

The upper boundary condition for the salinity equation was the flux of salt into an initially isohaline ocean. However, some insight into the time dependent behavior of the model can be gained from the analysis of a more idealized situation, one where the upper layer of an initially salt-free ocean of infinite depth is raised to a constant value S^* . Neglecting the effects of advection, horizontal diffusion, and convective adjustment the salinity equation (2.9) and its initial and boundary conditions become

$$\frac{ds}{dt} = k_s \frac{ds}{dz^2}, \quad (3.1)$$

$$S(t, 0) = \text{CONSTANT} = S^* \text{ for } t > 0, \quad (3.2)$$

$$S(0, z) = 0. \quad (3.3)$$

To solve equation (3.1) two new variables τ and γ are defined as

$$\gamma = k_s t, \quad (3.4)$$

$$\tau = \frac{z}{2\sqrt{\gamma}} = \frac{z}{2\sqrt{k_s t}}. \quad (3.5)$$

Transforming (3.1) into τ and σ space gives

$$\frac{ds}{d\tau} = -\frac{1}{4\tau} \frac{d^2s}{d\sigma^2}. \quad (3.6)$$

Assuming that S depends on time t only through σ implies that

$$\frac{ds}{d\tau} = \frac{ds}{d\sigma} \frac{d\sigma}{d\tau} = \frac{ds}{d\sigma} \left(-\frac{1}{4\tau\sqrt{\tau}} \right), \quad (3.7)$$

or that

$$\frac{ds}{d\tau} = -\frac{\sigma}{2\tau} \left(\frac{ds}{d\sigma} \right). \quad (3.8)$$

Substitution of this result into equation (3.6) gives

$$\frac{d^2s}{d\sigma^2} = -2\sigma \frac{ds}{d\sigma}. \quad (3.9)$$

Letting $g = \frac{ds}{d\sigma}$ yields

$$\frac{dg}{d\sigma} = -2\sigma g, \quad (3.10)$$

whose solution is well known as

$$g = g_0 e^{-\sigma^2}. \quad (3.11)$$

Further integration of (3.9) gives

$$s = s^* + \int_0^\sigma g_0 e^{-y^2} dy \quad (3.12)$$

where

$$S^* = S(r=0) = S(z=0), t > 0. \quad (3.13)$$

Finally the solution becomes

$$S(r) = S^* + \int_0^r q_0 e^{-y^2} dy \quad (3.14)$$

where S^* is the value of S at $r=0$.

The value of q_0 is determined from equation (3.3) as follows:

$$S(0, z) = S(\infty) = 0 \quad \text{for } z > 0, \quad (3.15)$$

from equation (3.14)

$$S(\infty) = S^* + q_0 \int_0^\infty e^{-y^2} dy = 0, \quad (3.16)$$

$$\text{since } \int_0^\infty e^{-y^2} dy = \sqrt{\pi}/2, \quad (3.17)$$

the final solution for q_0 becomes

$$q_0 = \frac{-2}{\sqrt{\pi}} S^* \quad (3.18)$$

and the solution of equation (3.1) including the boundary condition becomes

$$S(r) = S^* (1 - \text{ERF}(r)) \quad (3.19)$$

where

$$ERF(\tau) = \frac{2}{\sqrt{\pi}} \int_0^{\tau} e^{-y^2} dy. \quad (3.20)$$

Figure 3.1 is a plot of equation (3.19) and was used to determine an estimate for the salinity relaxation time. From this graph it was clear that $\tau = 0$ gives $S = S^*$, the true steady state solution; however, since both the depth, z , and the vertical diffusion coefficient for salt, k_s , were nonzero, a true steady state would exist only as time approached infinity. To avoid ambiguity, it was convenient to define a quasi-steady state to exist when $S \sim 0.9 S^*$ which corresponded to a τ value of 0.1. Solution of equation (3.5) for t gives the time required for the level z to be affected,

$$t = \frac{z^2}{4k_s \tau^2}. \quad (3.21)$$

Since t varied directly as the square of the depth, the salinity relaxation time was expected to be very long for the lower layers. For $k_s = 0.1 \text{ cm}^2 \text{ sec}^{-1}$ and $\tau = 0.1$ the first layer at five meters computed to be steady state in 0.2 years, the third in 20 years, the fifth in 500 years, and the seventh in 32,000 years. As the model was integrated over the relatively short period of 30 years, theoretically only the first 90 meters were expected to be in equilibrium. Furthermore, since the upper boundary condition

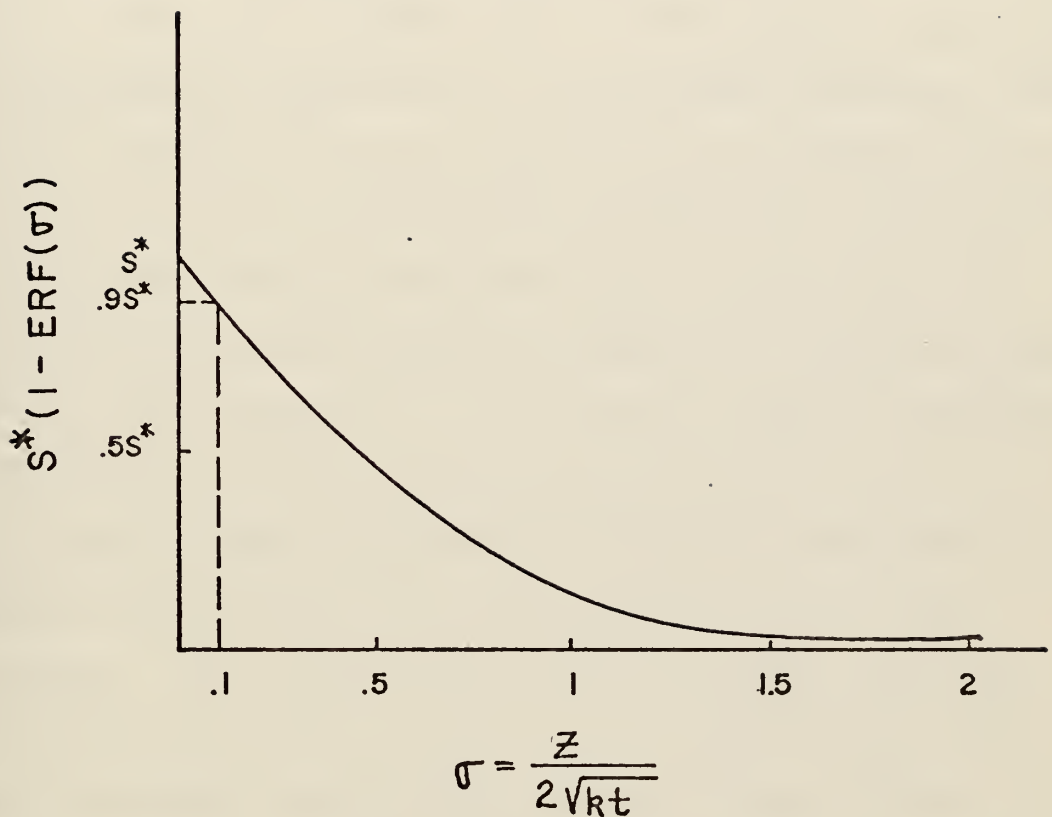


Figure 3.1 A plot of S^* vs. $\sigma = z/(2\sqrt{kt})$; the dotted line shows a quasi-steady state value of $0.9S^*$.

was the specification of the flux of salt and not the idealized condition treated above, the relaxation time was expected to be even larger for each level than indicated by (3.21).

Figure 3.2 is the salinity anomaly vs. time plot at various levels for a 30-year period at the grid point $I=10$, $J=13$, (see figure 3.20). This location was chosen for studying the dependence of the salinity relaxation time upon the vertical diffusion because the prescribed upward flux of salt at the surface was a maximum here. Additionally, because both the horizontal and vertical currents were small with little shear, the effects of advection were expected to be negligible. The apparent breaks at approximately 10 years in the otherwise smooth curves were caused by a change in k_M , the vertical diffusion coefficient for momentum, and did not affect the general nature of the adjustment. As predicted from the theoretical analysis, levels above 100 meters appeared to be approaching steady state and showed little change during the last 10 years of integration; however, levels below 250 meters showed a constant rate of increase of approximately 0.002°C per century at the end of the integration. Although the salinity at the lower levels was not in steady state, it was felt that this was not a serious problem because the salinity gradient did not have a significant effect upon the model dynamics, which were primarily controlled by the surface wind stress and the near surface eddy momentum transfer processes.

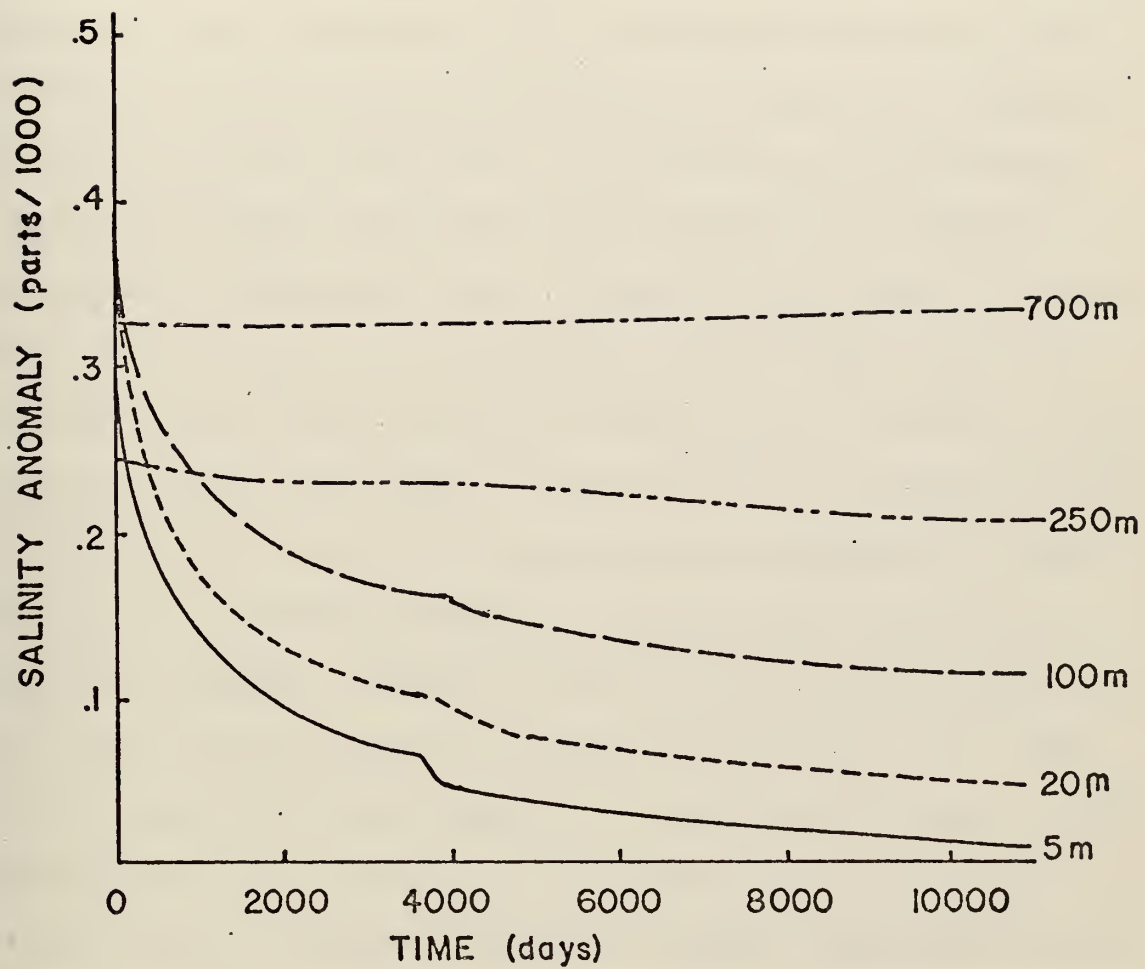


Figure 3.2 A plot of salinity vs. time at the grid point with maximum upward surface flux for levels 5, 20, 100, 250, and 700 meters. The ordinate values have been shifted to place all curves on one graph and only the slopes are significant.

2. Temperature Relaxation Time

As discussed in Section II, the upper boundary condition for temperature was quite different than the one for salinity. The flux of salt at the ocean surface was specified as a function of the existing salinity and the difference between the fixed rates of evaporation and precipitation (equation 2.50). If there were no horizontal transport of salt, a steady state could not be reached. Because the prescribed flux is nearly independent of salinity, those regions with precipitation excesses would tend to become less salty, whereas those with net deficits would tend to become more salty. Temperature, on the other hand, was different because the ocean surface temperature was tied to the apparent atmospheric equilibrium temperature $T_A^* = T_A + Q_1/Q_2$ (equation 2.49). If the temperature of the near surface layer T_1 became much different than T_A^* , then a large heat flux resulted which drove T_1 towards T_A^* and resulted in a reduction of the heat flux. If there were no horizontal transport of heat, a steady state could eventually exist in which the temperature of the ocean was everywhere equal to T_A^* . For these reasons, it was apparent that the theoretical analysis just performed applied more closely to temperature than to salinity. Accordingly, it was expected that the time required to reach temperature equilibrium would be less than that needed for salinity to reach steady state. To decrease the temperature relaxation

time, an initial temperature lapse rate of $-1^{\circ}/100$ meters was chosen, a value that was approximately equal to the steady state lapse rate in the equatorial domain of Haney's (1971) model.

Figure 3.3 shows the temperature vs. time plots for several levels at the same point as in figure 3.2. As expected, the near surface levels reached steady state comparatively quickly, whereas the deeper ones did not reach equilibrium over the 30-year integration period. The upper four levels achieved equilibrium after only 10 years and then showed little change for the next 20 years, whereas the corresponding salinity values, although approximately steady state, still continued to show some rate of change over the corresponding period. At the end of 30 years, the bottom ocean levels appeared to be warming at a constant rate of 0.25°C per century. This same trend was noted in Bryan's model (1968) although his time integration was carried out over a much longer time span. As in Bryan's model, the gradual heating was probably due to the selection of too cold of initial temperatures for the lower layers. Again as for salinity, the failure to reach steady state in the bottom layers was not felt to be especially damaging to the dynamical results obtained. The circulation was determined to be primarily wind-driven, and it is the surface layers which are of major interest in an ocean forecasting model.

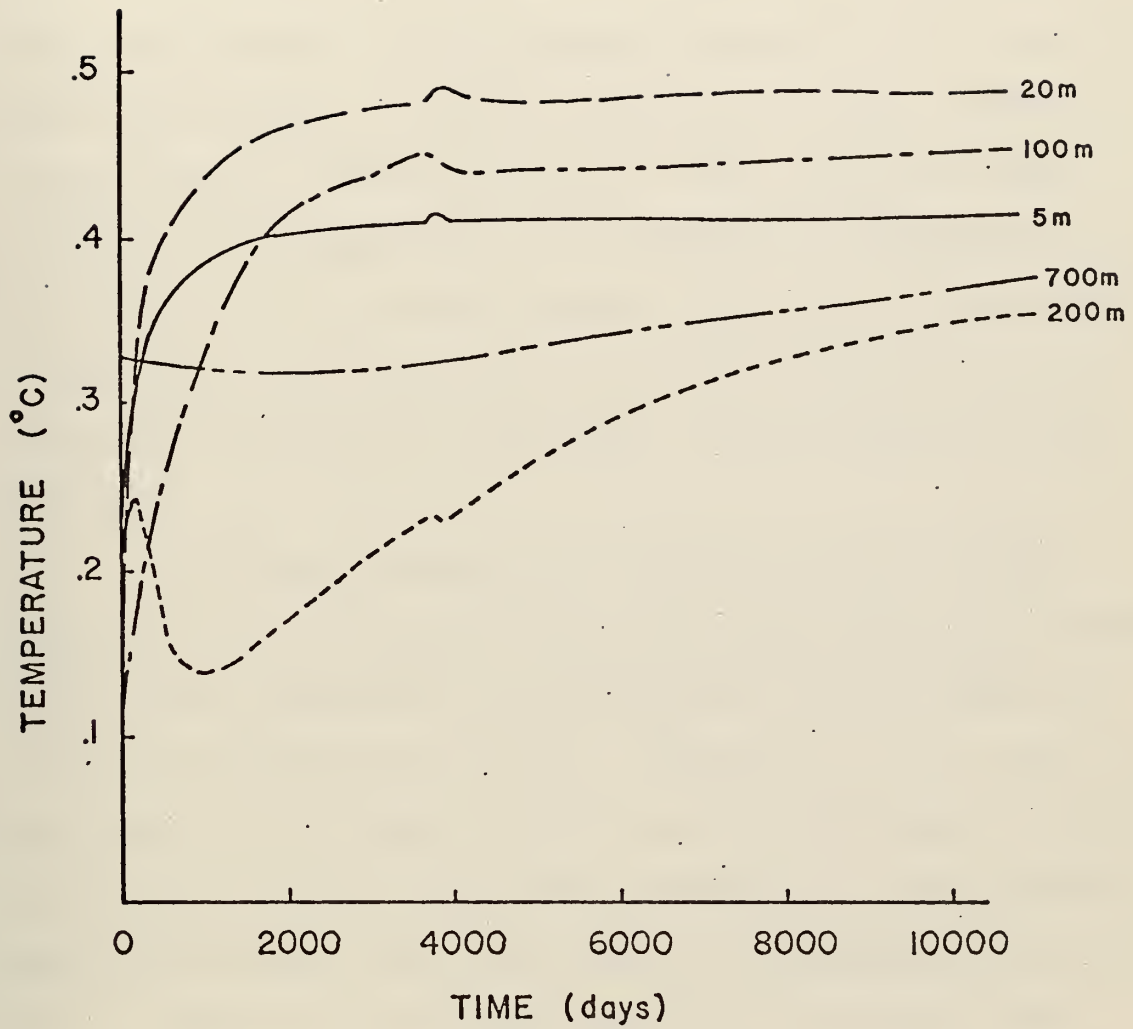


Figure 3.3 Temperature vs. time plots for levels 5, 20, 100, 250, and 700 meters over a 30-year period. The ordinate values have been transformed various amounts to place all curves on one plot and only the slopes are significant.

3. Dynamic Current Relaxation Time

Munk (1950), Charney (1959), Veronis (1959), and other researchers have proved that the wind plays an important role in determining the large scale features of the ocean circulation. It is generally known that the negative zonal wind stress in the near equatorial region causes a strong surface current towards the west, and that Ekman divergence is responsible for a meridional component of circulation at the surface towards each pole. Additionally, it has been established that the ocean response time to the surface stresses is very short, approximately 100 to 200 days.

No formal mathematical analysis of the current response time is attempted here, and only the actual results of the time integration are presented to verify that the dynamic response time is small. Figures 3.4, 3.5, and 3.6 are plots of the zonal current taken at the equator midway between the eastern and western boundaries. The computer analyzed data was taken from the time integration every 25 days. Figure 3.4 is representative of the second level below the surface where a strong countercurrent toward the east of 180 cm/sec had developed during the first 10 years. Figure 3.5 shows the flow at 100 meters where a sizeable countercurrent continued to exist after adjustment of k_M . Figure 3.6 is the zonal current vs. time at 700 meters and represents typical deep ocean water. The response time of

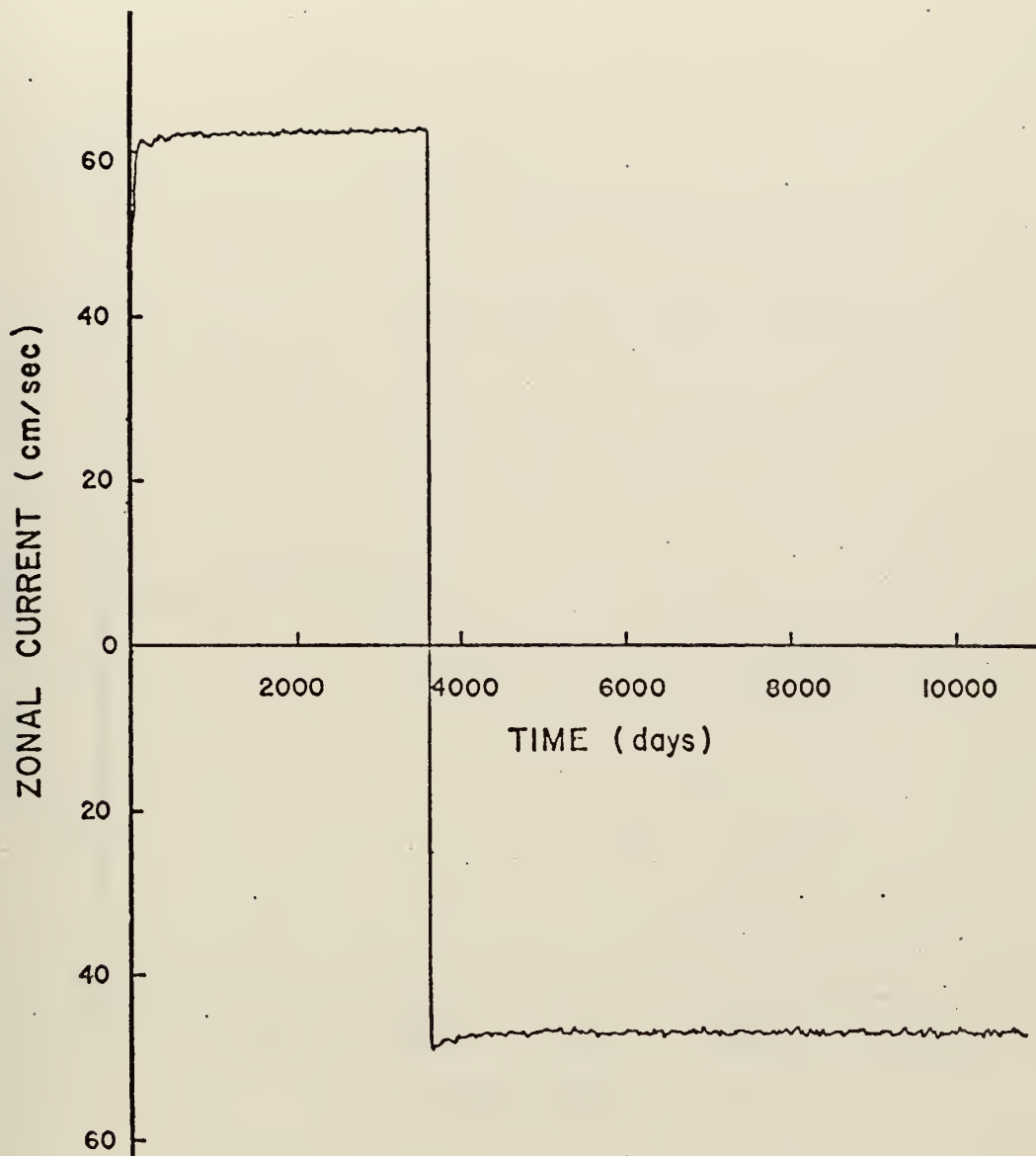


Figure 3.4 A plot of zonal current vs. time at the grid point $I=10$, $J=9$ located on the equator midway between the eastern and western boundaries. The depth is 20 meters.

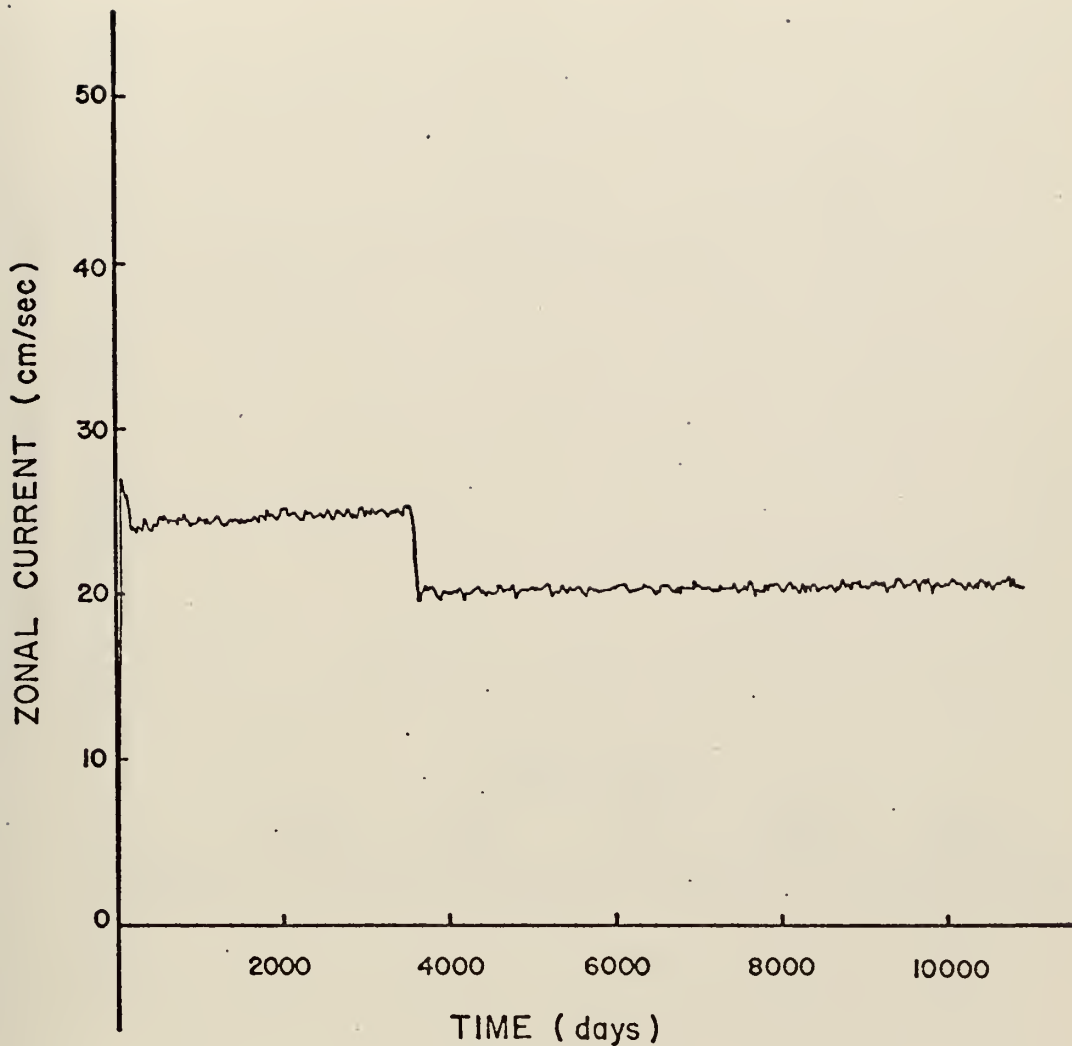


Figure 3.5 Zonal current μ (cm/sec) vs. time for grid location $I=10, J=9$ at 100 meters.

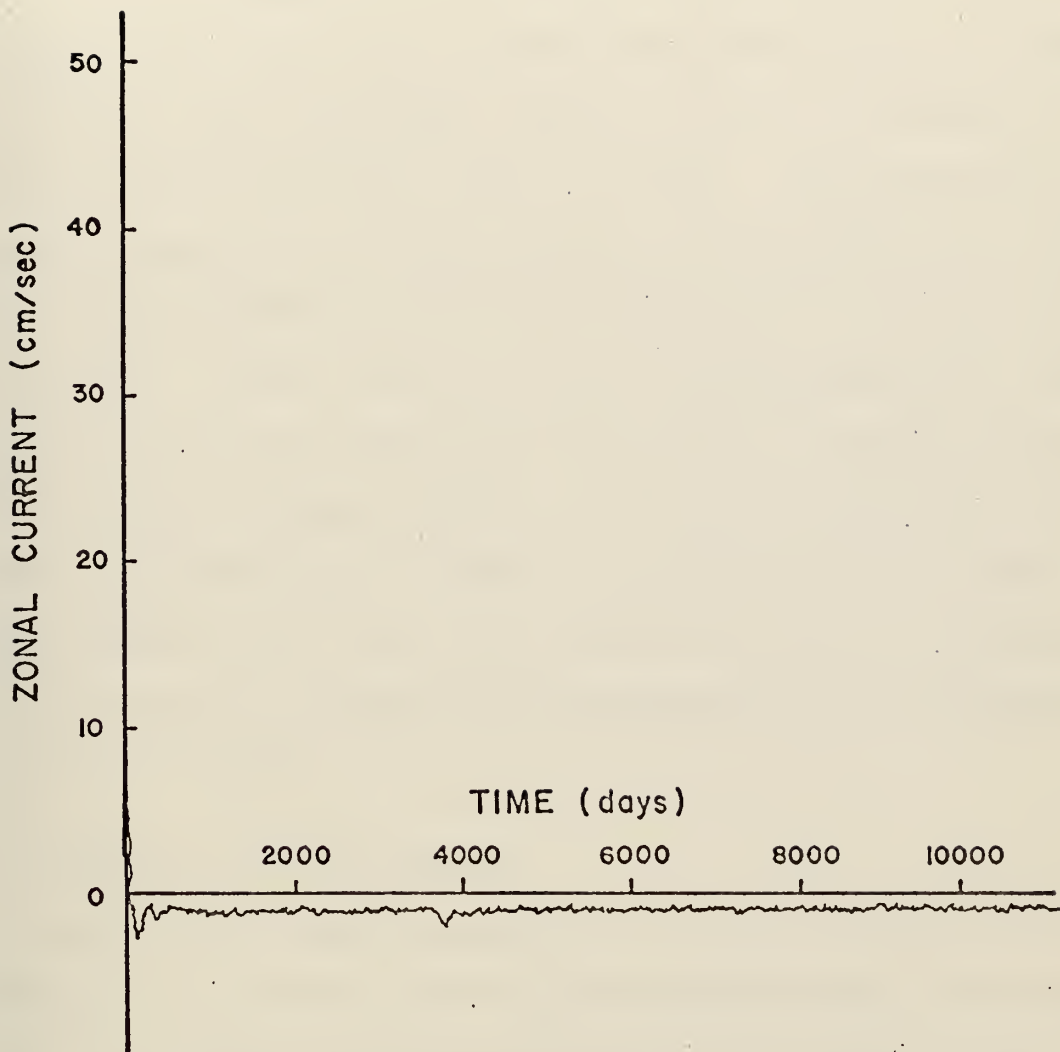


Figure 3.6 Zonal current u (cm/sec) vs. time at grid point $I=10$, $J=9$ at 700 meters.

about 100 days was extremely fast compared to those of salinity and temperature and appeared to be independent of depth.

The rapidity with which the wind-driven circulation adjusts was dramatically demonstrated after k_M was altered to correct two unrealistic features of the circulation that had appeared during the first 10 years. An unreasonably strong equatorial surface current had developed, and its associated countercurrent was located only 20 meters below sea level. Within 100 days after increasing k_M , the currents at most levels had adjusted to new values radically different from the previous values. At 20 meters the flow shifted from 60 cm/sec from the west to 47 cm/sec from the east. Additionally, the core of the countercurrent now appeared at 100 meters, a depth more representative of its position in the real ocean.

B. EQUATORIAL UNDERCURRENT

One of the unique features of the Pacific Ocean is the existence of a thin, swift countercurrent which is symmetric about the equator and moves eastward below the westward flowing South Equatorial Current. This phenomena, called the Cromwell Current, was first studied in detail by Knauss (1960) who determined the current to be about 300 km wide, approximately 200 m thick, and with velocities as high as 150 cm/sec. The core, a jet-like structure with stronger shear above its center than below it, was found to extend

over at least 3500 n mi at a depth that varied from 100 meters at 140°W, to about 75 meters near the Galapagos Islands. In a later study Knauss (1966) found a much weaker flow, and concluded that the countercurrent probably exhibited considerable year-to-year variability. He theorized that as a first approximation, the countercurrent could be considered as a separate flow imbedded in the surface South Equatorial Current. A stronger than average surface current was thought to be accompanied by a weaker undercurrent, whereas a weaker surface current was believed to be associated with a stronger than average undercurrent.

Several theoretical analyses of the Cromwell Current have been performed. Charney (1959) showed that for a homogeneous ocean driven by a uniform wind, the zonal current profile was parabolic with the maximum velocity dependent upon the coefficient of vertical eddy viscosity ν . For large values of ν the easterly surface current extended to the hypothetical level of no motion. As ν was allowed to decrease, the countercurrent began to develop; however, at very small values of ν , the countercurrent became so well developed that the flow at the surface had reversed and become westerly. Veronis (1959) offered a simplified explanation of the undercurrent using the idealized basin shown as figure 3.7. He reasoned that a surface wind blowing from the east caused an accumulation of water at the western boundary, which caused the pressure gradient to drive the

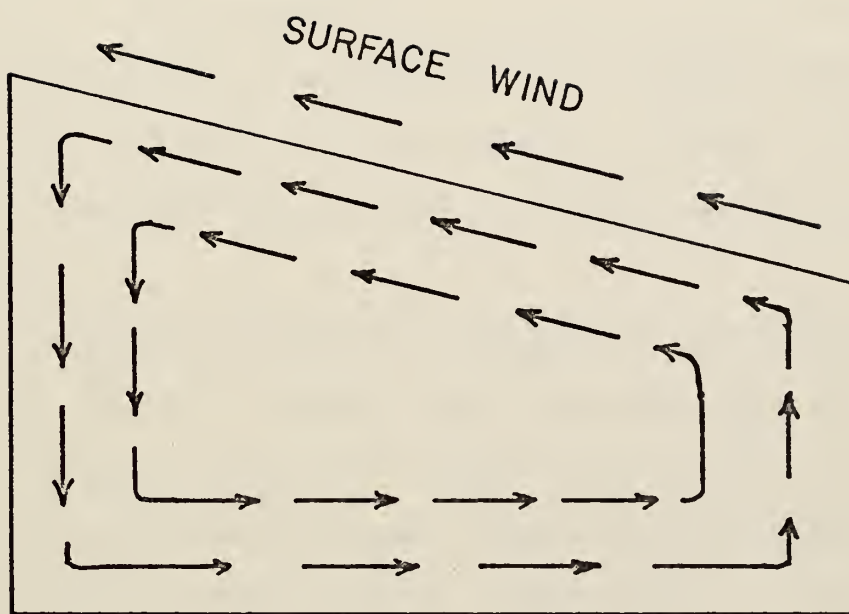


Figure 3.7 (After Veronis) A cellular circulation develops when a nonrotating basin is subjected to a surface wind stress; the increased pressure at the western boundary causes an eastward countercurrent to exist below the westward surface current.

subsurface water towards the east. Arthur (1959), by neglecting all terms in the x -component equation at the equator except the pressure gradient and frictional stress ones, showed that a representative zonal profile containing a countercurrent could be calculated from values of surface current velocity, wind stress, and pressure gradient for a constant u . Additionally, he concluded that although the solution was stable, the nonlinear terms $\frac{\partial u}{\partial x}$ and $\frac{\partial u}{\partial z}$ were probably not negligible. Unfortunately, inclusion of the nonlinear terms would have made the analytical analysis difficult.

In an equatorial prediction model with good vertical resolution near the surface, the equatorial countercurrent should be readily resolved. Figure 3.8 is an E-W cross section of zonal current taken along the model equator at the end of the 30 years of time integration. A countercurrent of about 20 cm/sec had developed at a mean depth of about 100 meters. This current appeared to be slightly more intense and at a greater depth near the western boundary than near the eastern boundary, and exhibited considerably more vertical current shear above the core axis than below it. Additionally, at approximately 700 meters the flow was toward the west, as it was at the surface. For comparison, the corresponding equatorial cross section for the Pacific after Knauss (1960) is shown as figure 3.9. Although the observed data exhibited considerable station to station

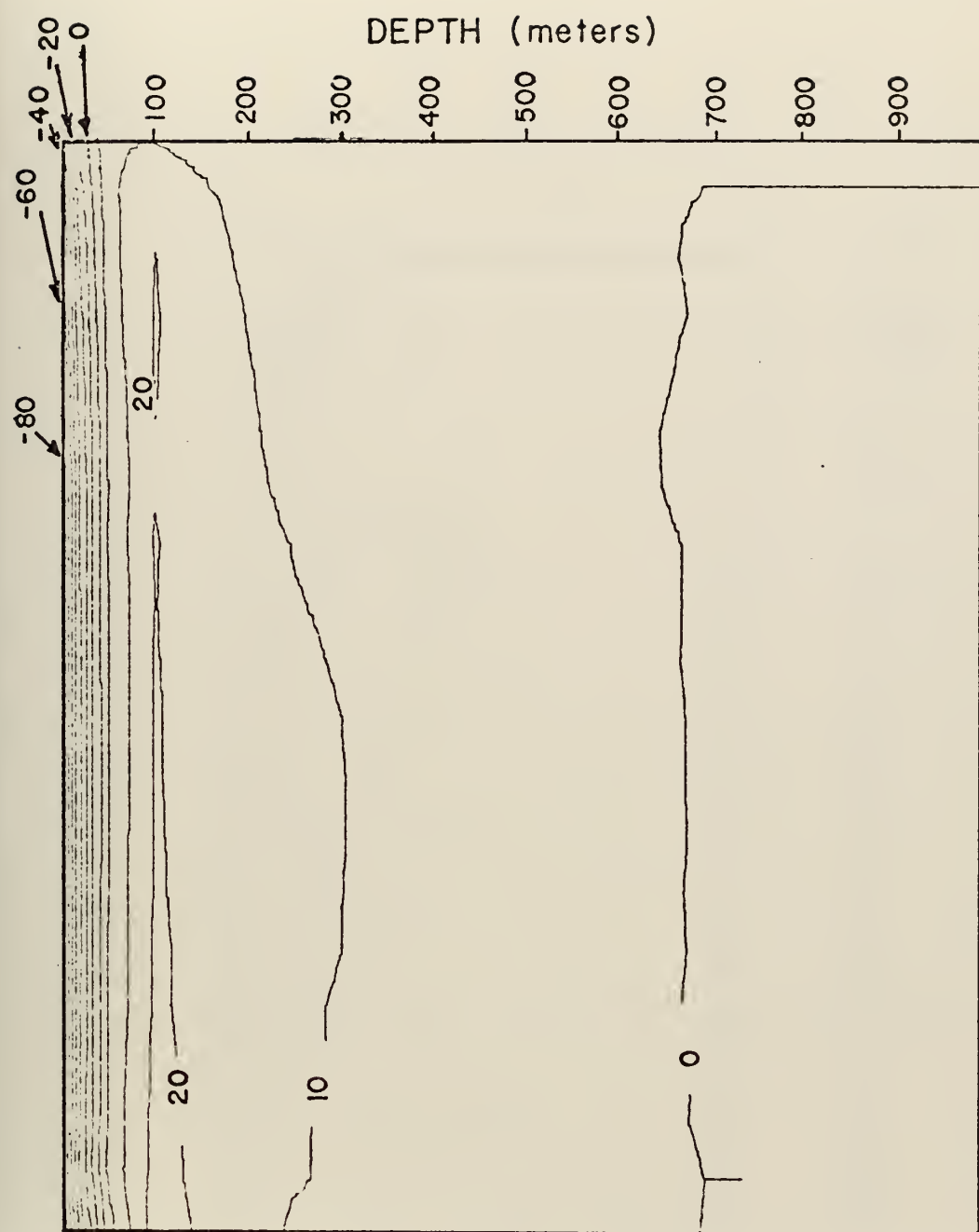
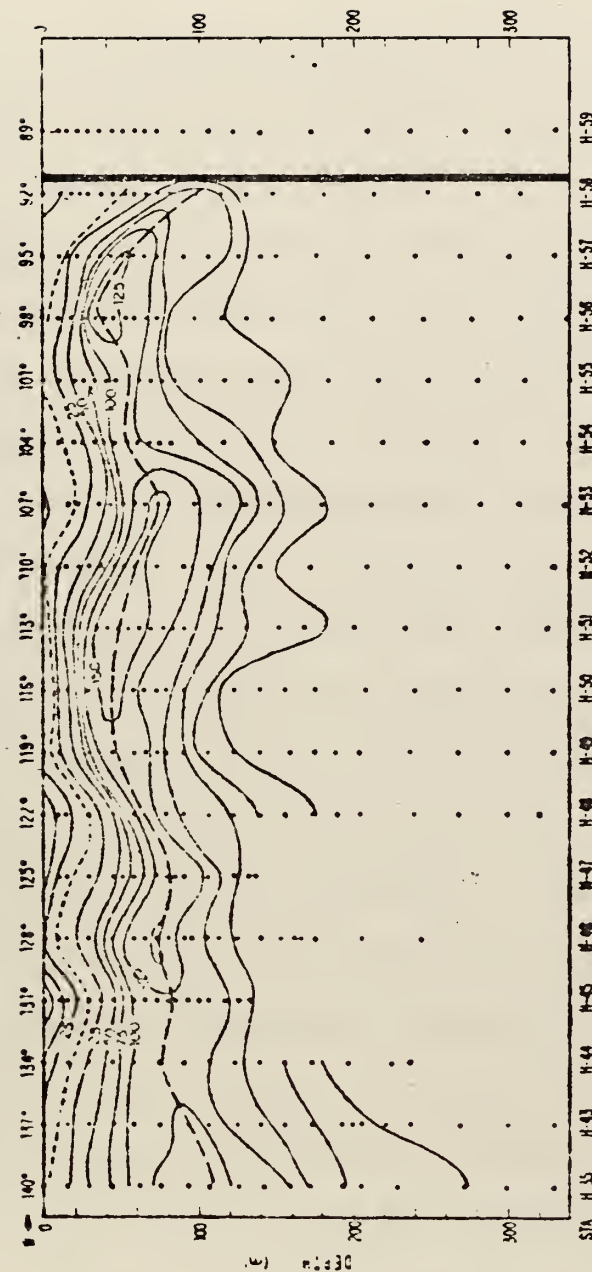


Figure 3.8 E-W cross section along the equator of u (cm/sec) vs. depth (meters) after 30 years of integration.



variability, all of the gross features are easily identified in the model. However, significant differences between the observational and model results were found to exist. The velocity of the Cromwell Current averaged about 140 cm/sec compared to the model mean value of 20 cm/sec. Also, the mean upward slope of the current core toward the east was somewhat greater in the Pacific cross section; this may be due to insufficient vertical resolution in the model.

As a further comparison, the vertical profile of the east-west averaged current in the model was plotted, (figure 3.10), with a typical Pacific profile determined by Knauss (1966). Although the magnitudes were quite different, the vertical current shear above the core of the undercurrent was quite similar, and both were approximately parabolic in agreement with Charney's theoretical results. Below the point of maximum velocity, the real data retained its parabolic shape, whereas the mathematical form of the model profile is not easily determined. One possible explanation for the difference in the profiles is that the mean surface winds during the observation period were below average. Then according to Knauss's concept of the undercurrent as a flow embedded in the surface current, the weaker-than-normal surface winds would have caused a below average surface flow and an above average countercurrent. Although this simple argument has some merit, a more likely explanation lies in the way vertical diffusion of momentum was handled in the model. The assumption of a constant kinematic

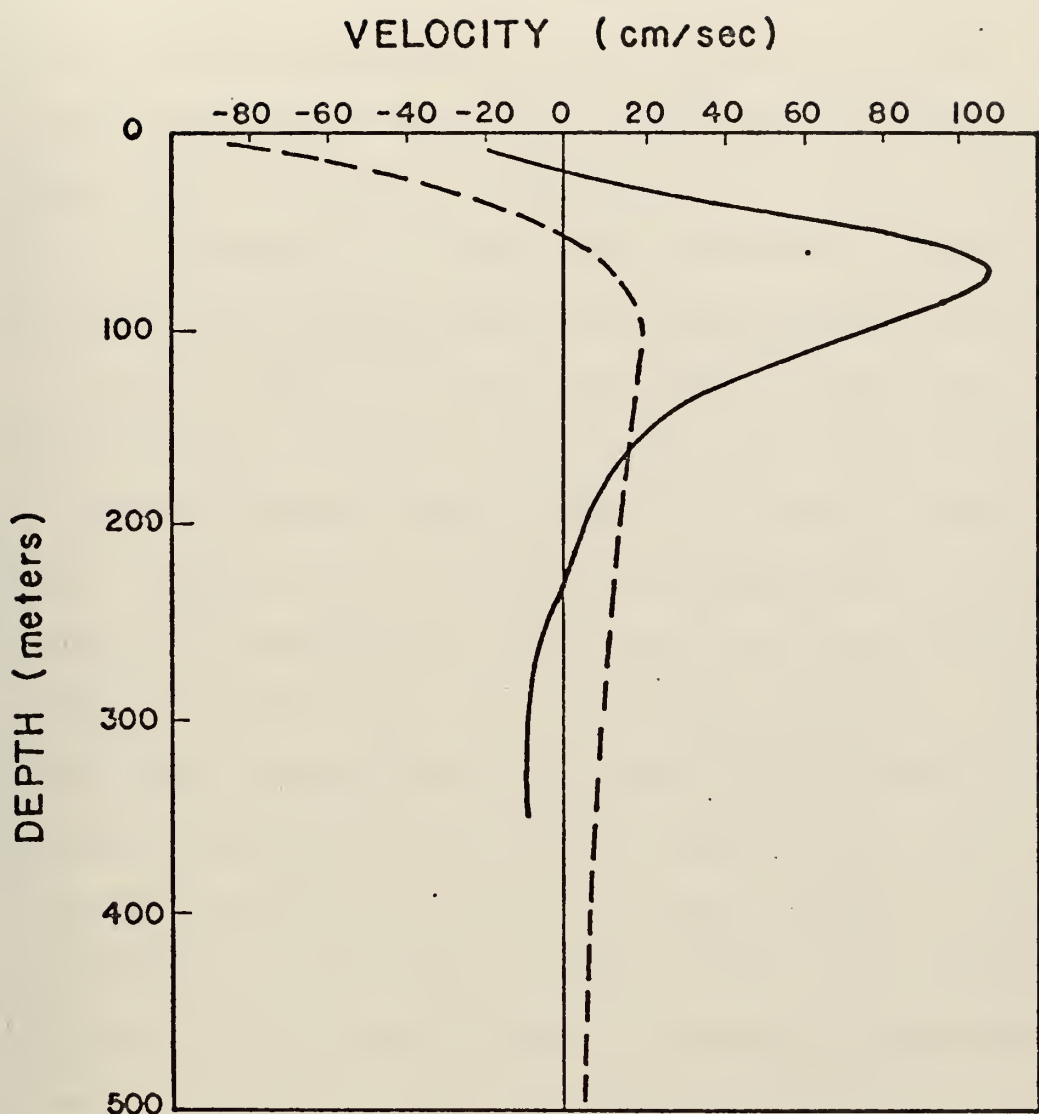


Figure 3.10 Plot comparing the average model zonal current shown by the dashed line with the smoothed zonal current at 118°W in the eastern tropical Pacific as determined by Knauss (1966). The model time is 30 years.

eddy viscosity, k_M , implied that the eddies that transfer momentum vertically are independent of depth. In the near surface layers of the ocean, k_M may increase toward the surface due to increased wind mixing, but the exact functional dependence of k_M on z is not clear. Also, k_M should depend upon the vertical stability of the water column as measured perhaps by a large scale Richardson number, but again the best formulation of the dependence is not known.

The jet-like structure of the model undercurrent was well displayed in a N-S cross section of zonal current taken approximately midway between the west and east boundaries (figure 3.11). The strong wind-generated surface current, its associated undercurrent, and the pronounced vertical current shear were all readily apparent. These significant features were also apparent in figure 3.12, a typical cross section taken by Knauss on his 1958 expedition, during which the current was the stronger of the two expeditions. Also shown on figure 3.12 is the thermal structure of the undercurrent. Although the isotherms showed considerable small scale spatial variations, the large scale pattern revealed that the isopleths were concave downward above the current core, whereas below it the concavity was reversed. In an attempt to identify a similar thermal structure in the model, the model countercurrent was superimposed on the N-S cross section of temperature (figure 3.13). A cold region above the undercurrent axis was evidenced by isotherms that were concave downward.

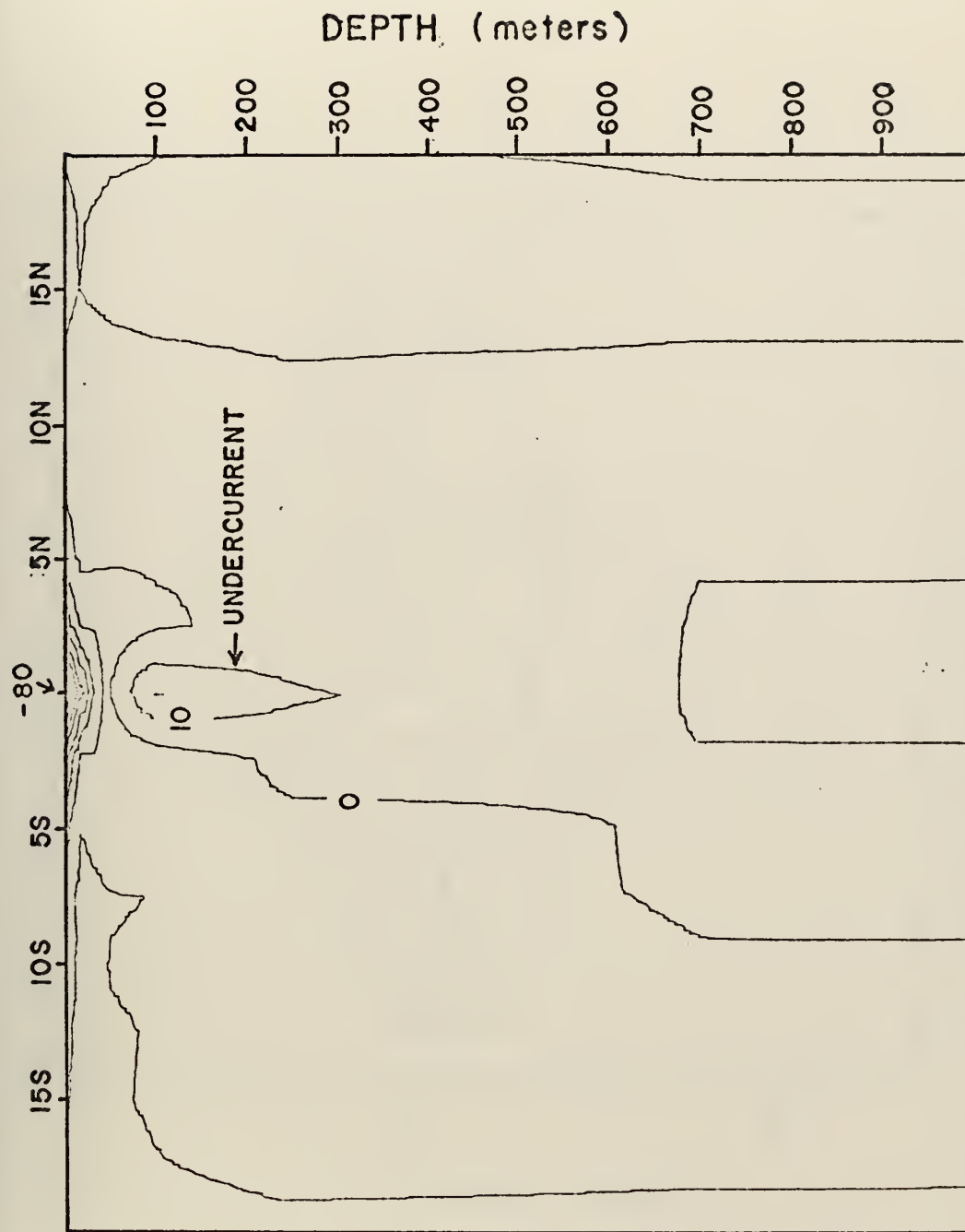


Figure 3.11 A N-S vertical cross section of zonal current at a location midway between the east and west boundaries at 30°S latitude. Easterly flow is negative, westerly flow is positive. The undercurrent is centered on the equator, where the horizontal velocity (u, v) is calculated.

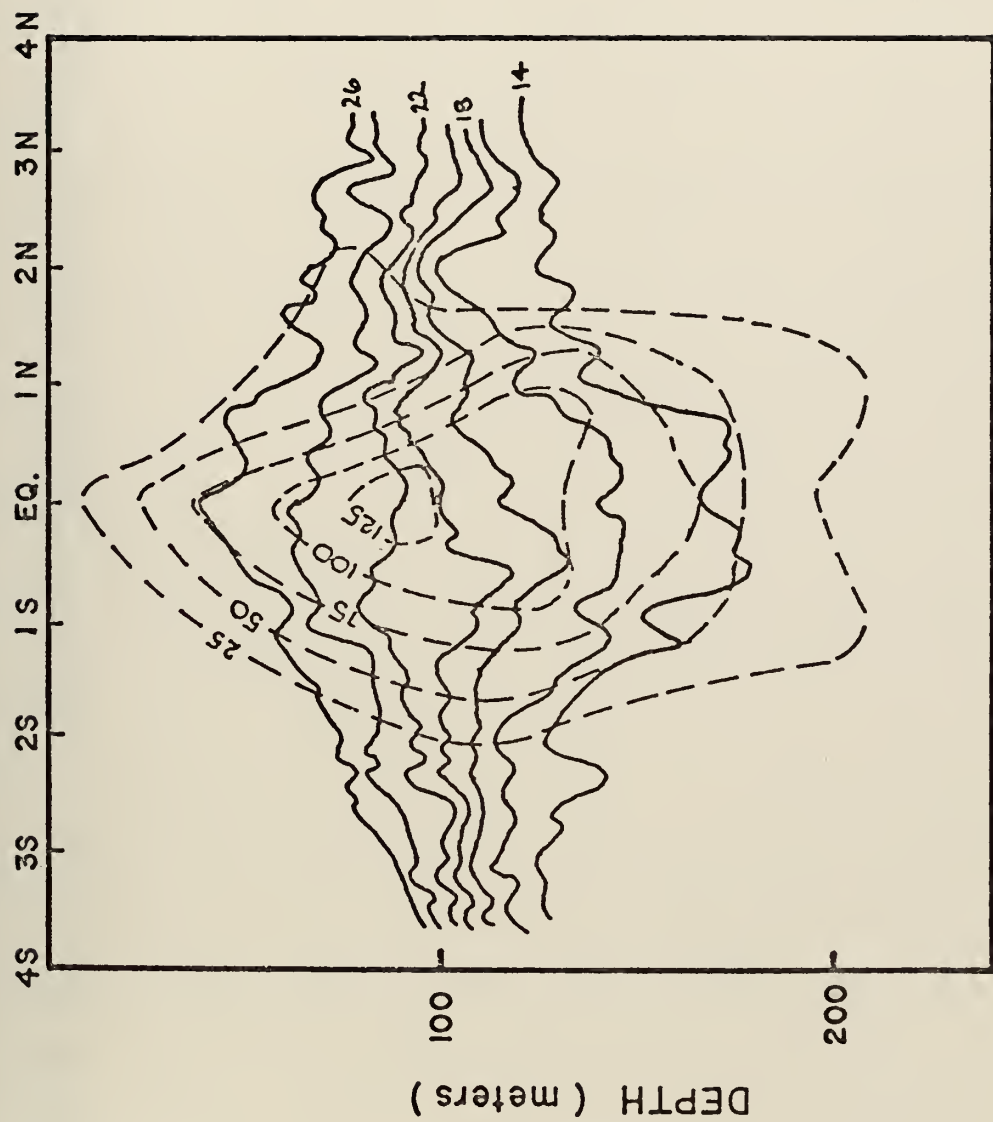


Figure 3.12 N-S cross section of zonal current (dotted lines, cm/sec) and the associated thermal structure (solid lines, °C) at 140°W for 20-22 April 1958 (after Knauss).

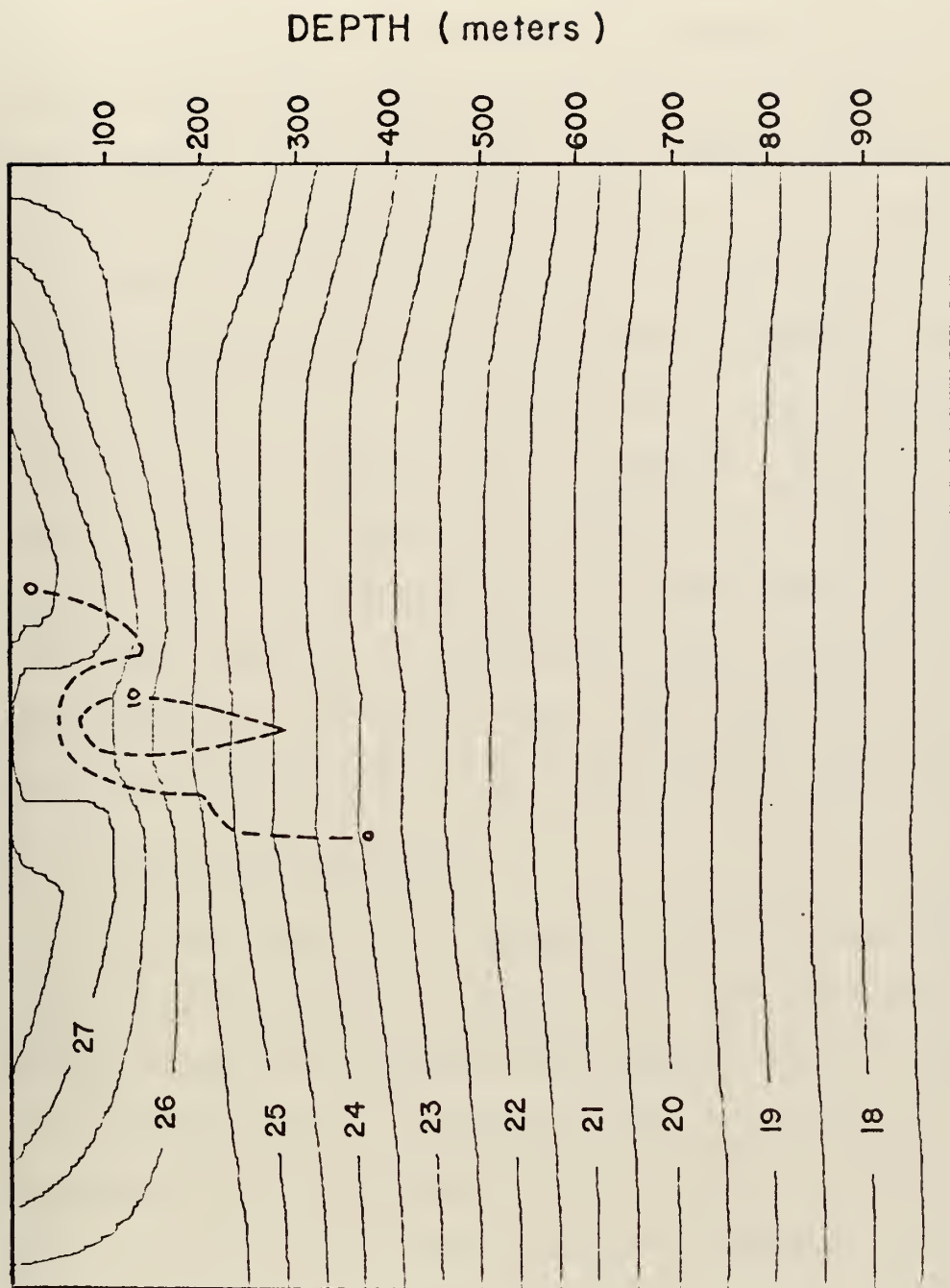


Figure 3.13 N-S cross section of temperature ($^{\circ}\text{C}$) at the midpoint between the eastern and western boundaries. The isotherms are solid lines at contour interval 0.5° C ; the dotted lines represent the model undercurrent.

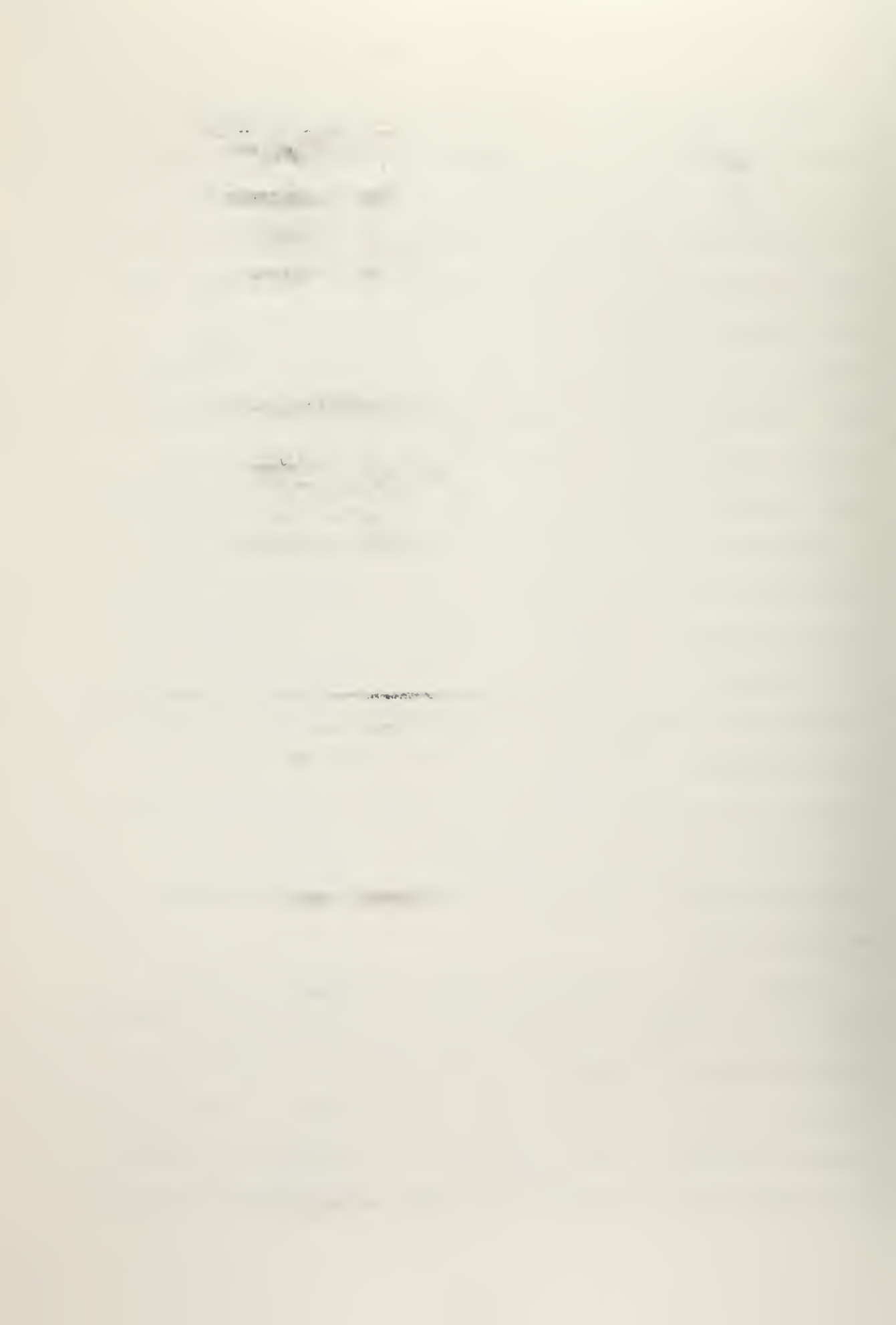
However, this same pattern persisted for 200 meters below the axis, where only a slight reversal in curvature was noted. The failure of the model to adequately resolve this thermal structure is most likely due to the simple form of the kinematic eddy viscosity. The thermal structure in the vicinity of the equator in figure 3.13 is adequately explained by vertical advection by a strong upward vertical velocity above about 300 m, and weaker downward motion below 300 m (figure 3.23). The equatorial isotherm spreading in the real ocean (figure 3.12) is probably caused by enhanced vertical mixing in the strong shear regions above and below the jet core. An important goal of any future research on this model should be to determine a more adequate vertical eddy diffusion coefficient, k_M ; one that is a function of vertical stability, vertical current shear, and depth.

C. CURRENT CIRCULATIONS

The model was driven primarily by the prescribed surface wind stress τ_x shown in figure 2.3. The existence of the single minimum of τ_x displaced slightly north of the equator is important, for it causes the curl of the wind stress to be greater in the northern domain. As Munk (1959) showed, this asymmetry would tend to cause a stronger circulation in the Northern Hemisphere, and the non-zero wind stress curl on the equator would cause a circulation gyre to exist there. To more fully discuss this last point the general circulation of the model as a whole will be described.

Figures 3.14 and 3.15 are the zonal and meridional current components at five meters and illustrate the general flow patterns. Near the equator a strong zonal current flow towards the west had been created. Because the coriolis force is exactly zero on the equator, there was little tendency for this current to flow laterally away from the equator and the meridional current component was essentially zero. Several degrees on each side of the equator a geostrophic plus friction balance tended to take place and Ekman divergence was evident. The zonal component decreased in magnitude and the meridional current increased as the surface mass transport tended to become essentially poleward in both northern and southern hemispheres. In response to the divergence of surface water, vertical upwelling of cool bottom water took place in the equatorial region to maintain mass continuity. The weak southward directed flow on the equator in the eastern half of the basin, and alternating north-south flow in the western half, is a part of the horizontal gyre driven by the curl of the wind stresses mentioned above.

Figure 3.16, a horizontal cross section of vertical velocity, w , showed the existence of a strong band of upwelling centered on the equator. This figure also showed the effects of the boundaries on the flow pattern. Along the eastern boundary, strong upwelling was necessary to replace the surface water carried west by the strong surface current;



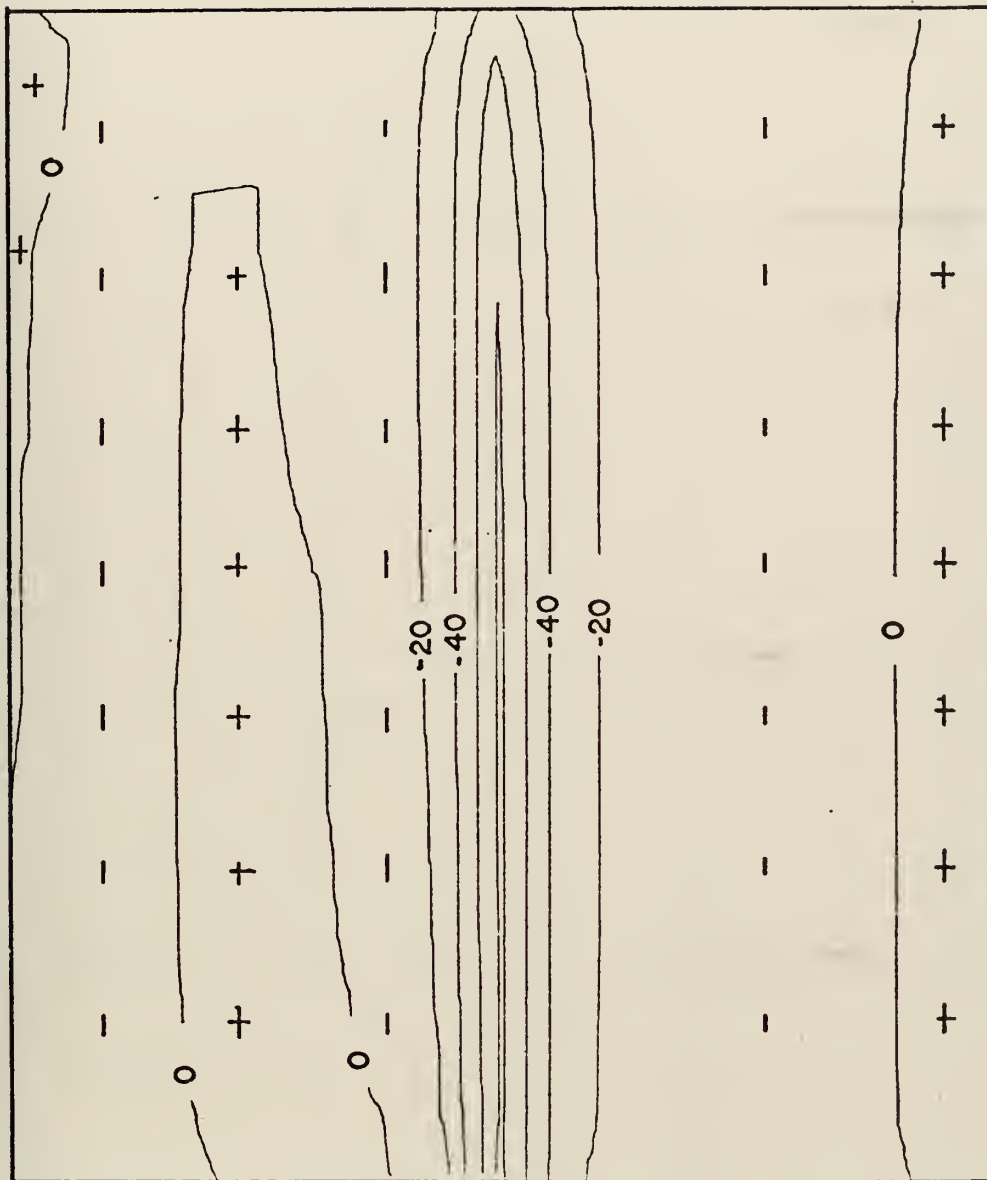


Figure 3.14 Horizontal cross-section of zonal current u (cm/sec) at a depth of 5 m after 30 years of time integration. Flow to the east is negative, to the west positive; the contour interval is 20 cm/sec.

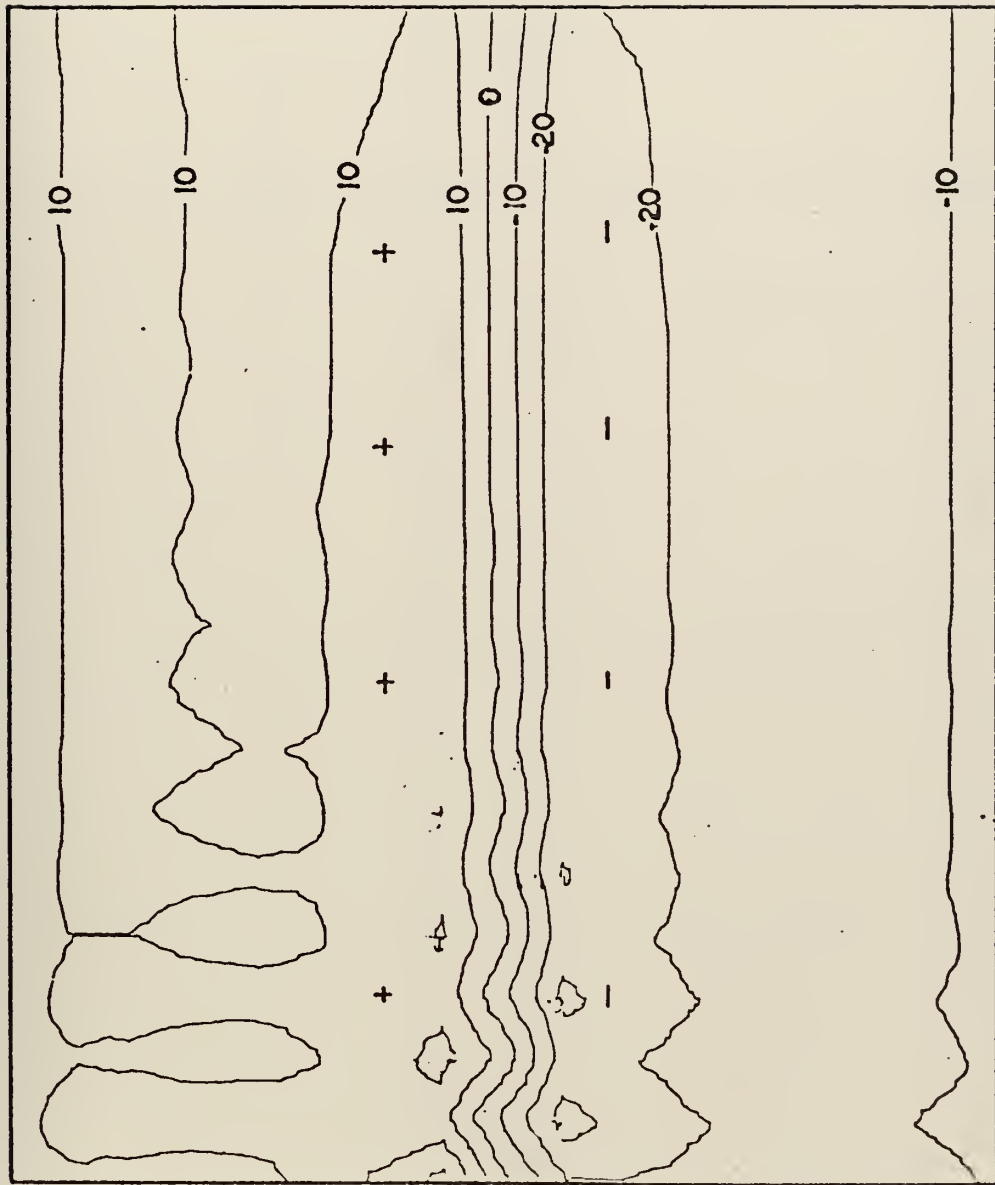


Figure 3.15 Horizontal cross section of meridional current v (cm/sec) at 5 meters after 30 years. The contour interval is 10 cm/sec.

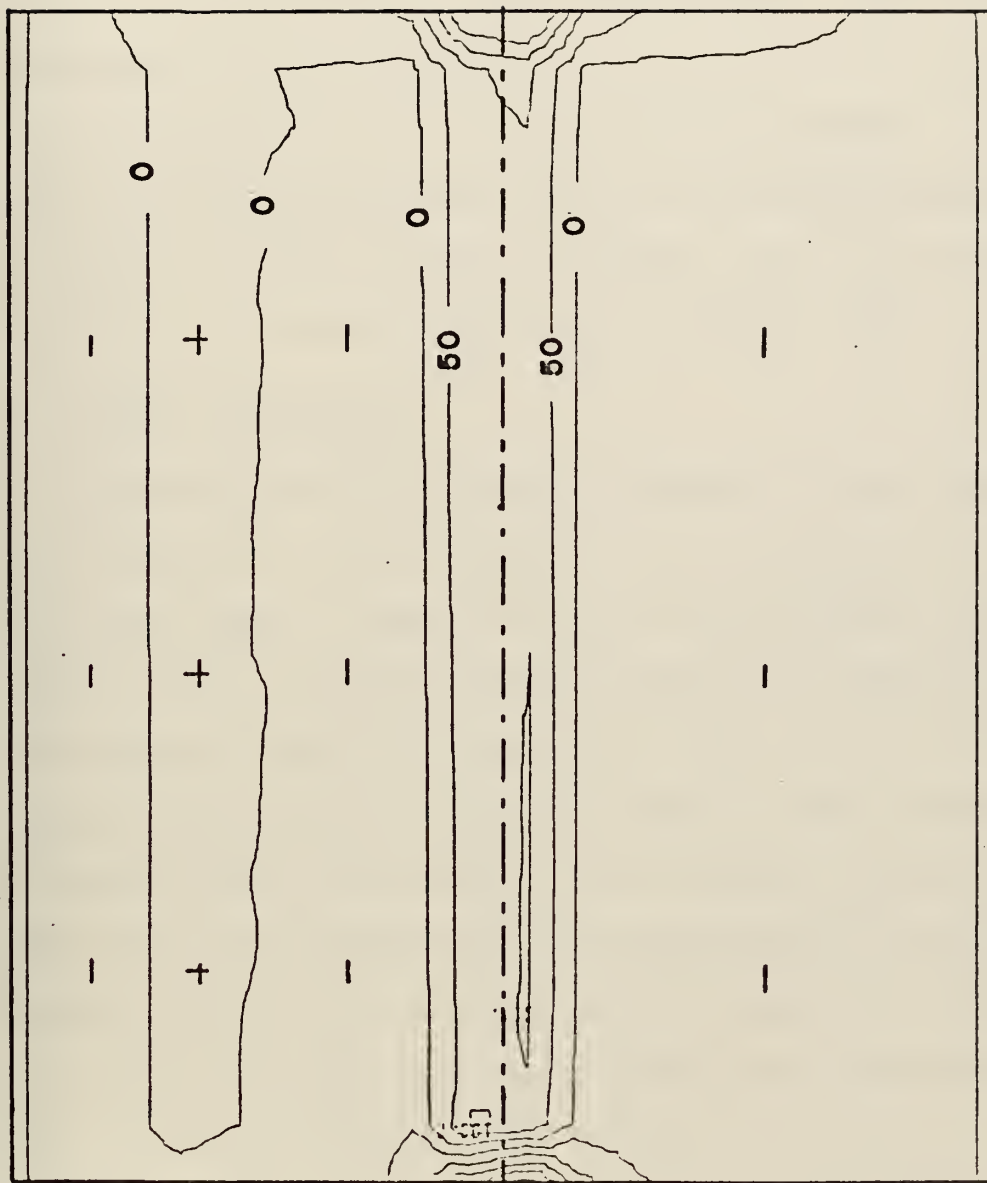


Figure 3.16 Horizontal cross section of vertical velocity w (cm/day) after 30 years. Positive values indicate upwelling, negative ones downwelling. The contour interval is 50 cm/day.

near the western boundary the large accumulation of surface water due to the surface current caused large downwelling. Near both northern and southern boundaries, strong downwelling was necessary to compensate for the poleward transport of surface water in both hemispheres. The nonuniform structure of the horizontal cross section of meridional current (figure 3.15) is caused by the presence of Rossby waves in the vertical mean part of the current that have propagated towards the west, impinged upon the western boundary, and become standing waves (Munk, 1950).

D. THERMAL STRUCTURE

Since the model was driven primarily by the surface wind stress, it was anticipated that the patterns of current flow would have a large effect upon the thermal structure. Figure 3.17, a horizontal cross section of temperature at five meters, showed this to be the case. A relatively cold tongue caused by upwelling was formed at the equator. This minimum was most pronounced at the eastern boundary where cold water was advected to the surface by the strongest vertical velocities. As this cooler water was transported to the west, it gained heat and the thermal gradient weakened. Two warm tongues were formed at 6 N and 9 S due to surface heating and weak sinking of the cool equatorial water after it had diverged from the equator. Further poleward movement of this equatorial water caused cooling as the amount of surface heating began to decrease.

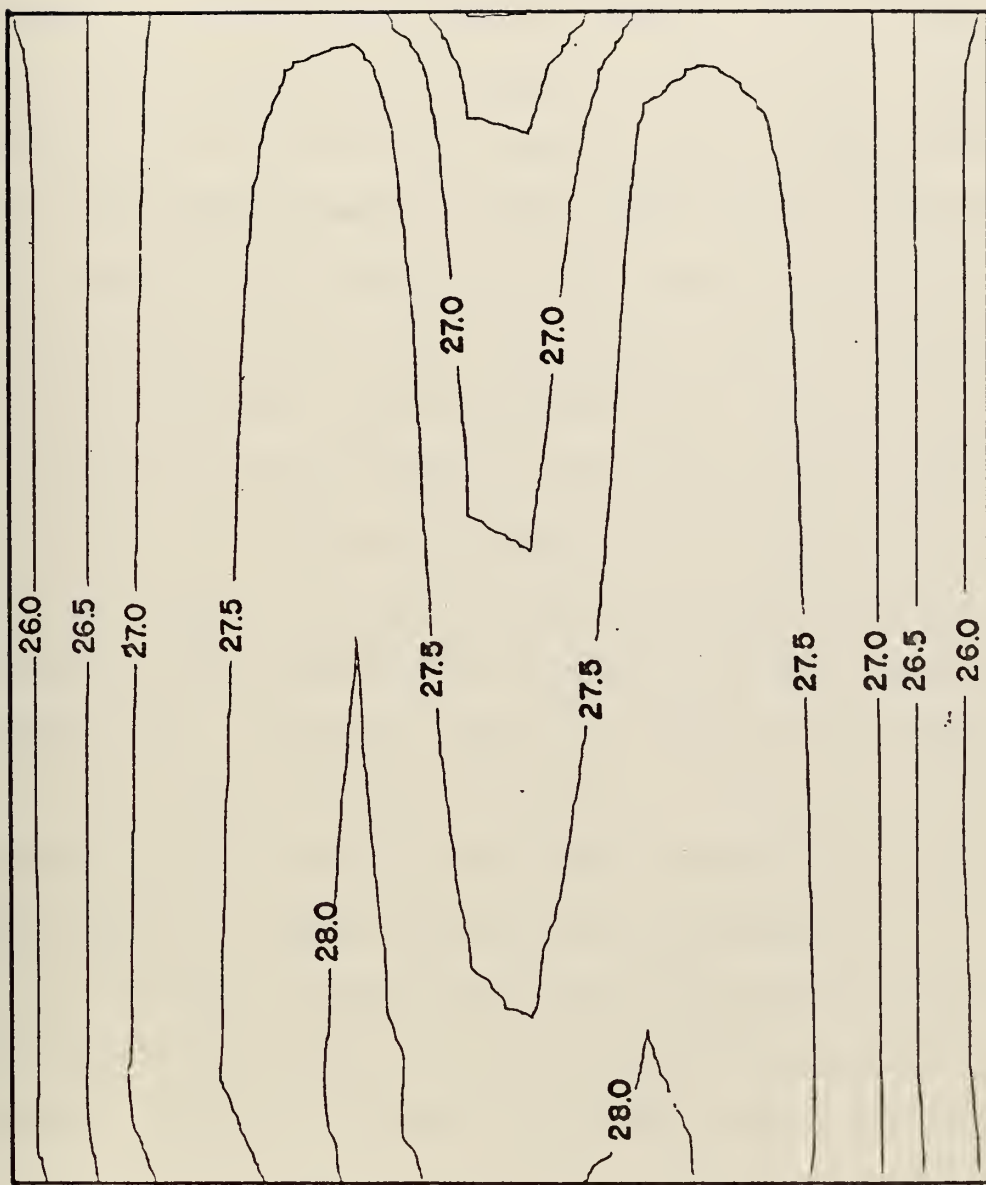


Figure 3.17 A horizontal cross section of temperature ($^{\circ}\text{C}$) at 5 meters for a contour interval of 0.5°C .

A realistic modeling of the vertical thermal structure is essential for any ocean model that is to be coupled to an atmospheric model for long range prediction purposes. Figure 3.18 is an E-W vertical cross section of temperature along the equator and showed a thermal gradient that was gravitationally stable. Except for the layers above 100 meters, which exhibited a nearly neutral temperature gradient, all layers showed a large stable lapse rate. The initial temperature gradient of -1°C per 100 meters had not changed appreciably over the 30 year time integration for levels below 200 meters. What appeared to be the top of the permanent thermocline existed at depths that varied from almost zero near the eastern boundary to about 100 meters near the western wall. The near isothermal temperatures normally found in real oceans at great depths had not developed appreciably. However, towards the end of the integration the two lower levels were warming at the rate of 0.25°C per decade, and it was felt that over a very long time period the desired result could have been realized.

To further examine the thermal structure, vertical profiles of temperature vs. depth at the three selected stations marked on figure 3.18 are shown as figure 3.19. The first station at 10° west of the eastern boundary showed no isothermal layer; equatorial upwelling had tended to force the characteristics of the deep water on the surface layers. The next station located at the midpoint between the boundaries showed the development of a near isothermal layer due

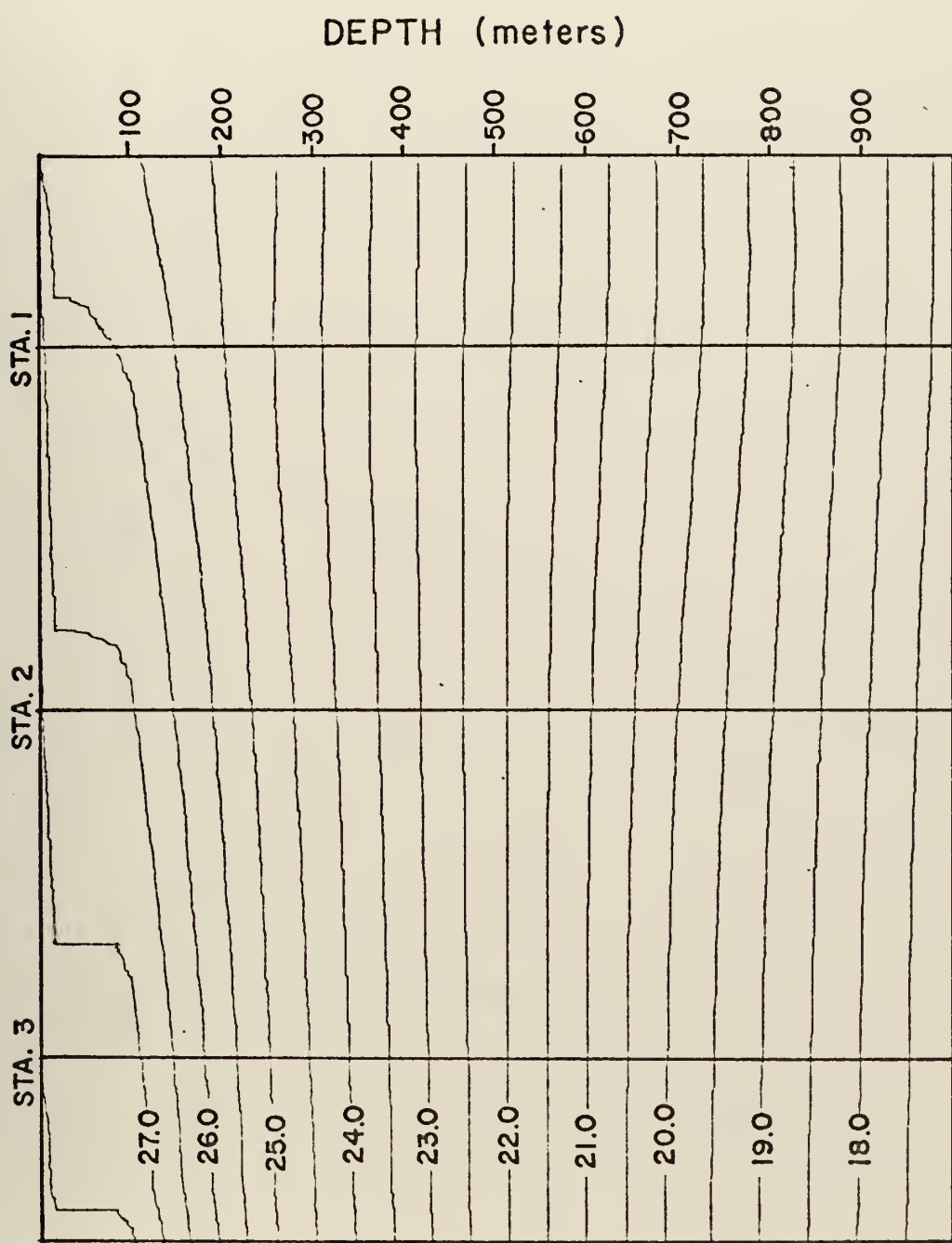


Figure 3.18 An E-W vertical cross section of temperature ($^{\circ}\text{C}$) along the equator for contour interval 0.5 $^{\circ}\text{C}$. The vertical lines are soundings plotted in figure 3.19. These three stations give a detailed look at the vertical thermal structure.

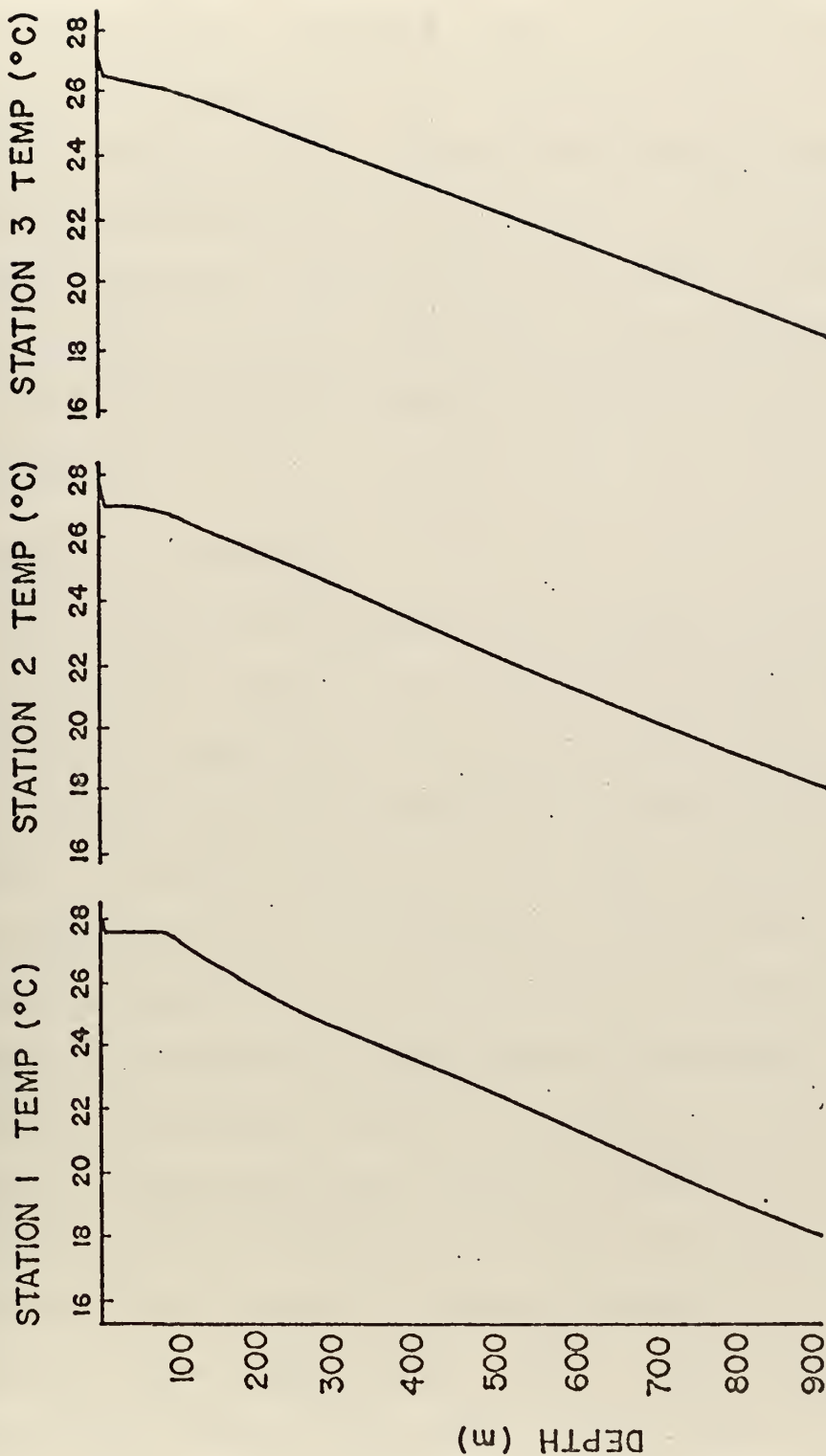


Figure 3.19 Vertical temperature profiles at three selected stations along the equator as marked on figure 3.18.

to the shallower vertical velocity pattern toward the west. Station number three located 10° east of the western boundary showed the deepest isothermal layer. All three profiles had a significant gradient between layers one and two, a distance of only fifteen meters. In the real ocean a weak wind would have been sufficient to mix this layer and establish isothermal conditions. One of the weak points of the present model is felt to be the lack of an effective modeling of surface wind mixing and internal vertical mixing in the stable case.

E. SALINITY STRUCTURE

The salinity distribution was largely determined by the upper boundary condition for salt which depended upon the net rates of evaporation and precipitation shown by figure 2.5. Figure 3.20 is the horizontal cross section of salinity anomaly, $(S\% - 34.0\%) \times 100$, at a depth of five meters. Although the net rate of evaporation minus precipitation curve was symmetric about the equator, the surface salinity pattern was asymmetric, which showed the strong role that advection and dynamics played. As shown by figure 2.5, two minima of evaporation rate minus precipitation rate were located at about 6° N and 6° S. If the ocean were completely motionless, two minima of salinity anomaly would tend to result at these locations, as the net rate of precipitation excess would tend to dilute the surface water. As seen from figure 3.20, both minima were shifted poleward by the meridional current components of both hemispheres. Between

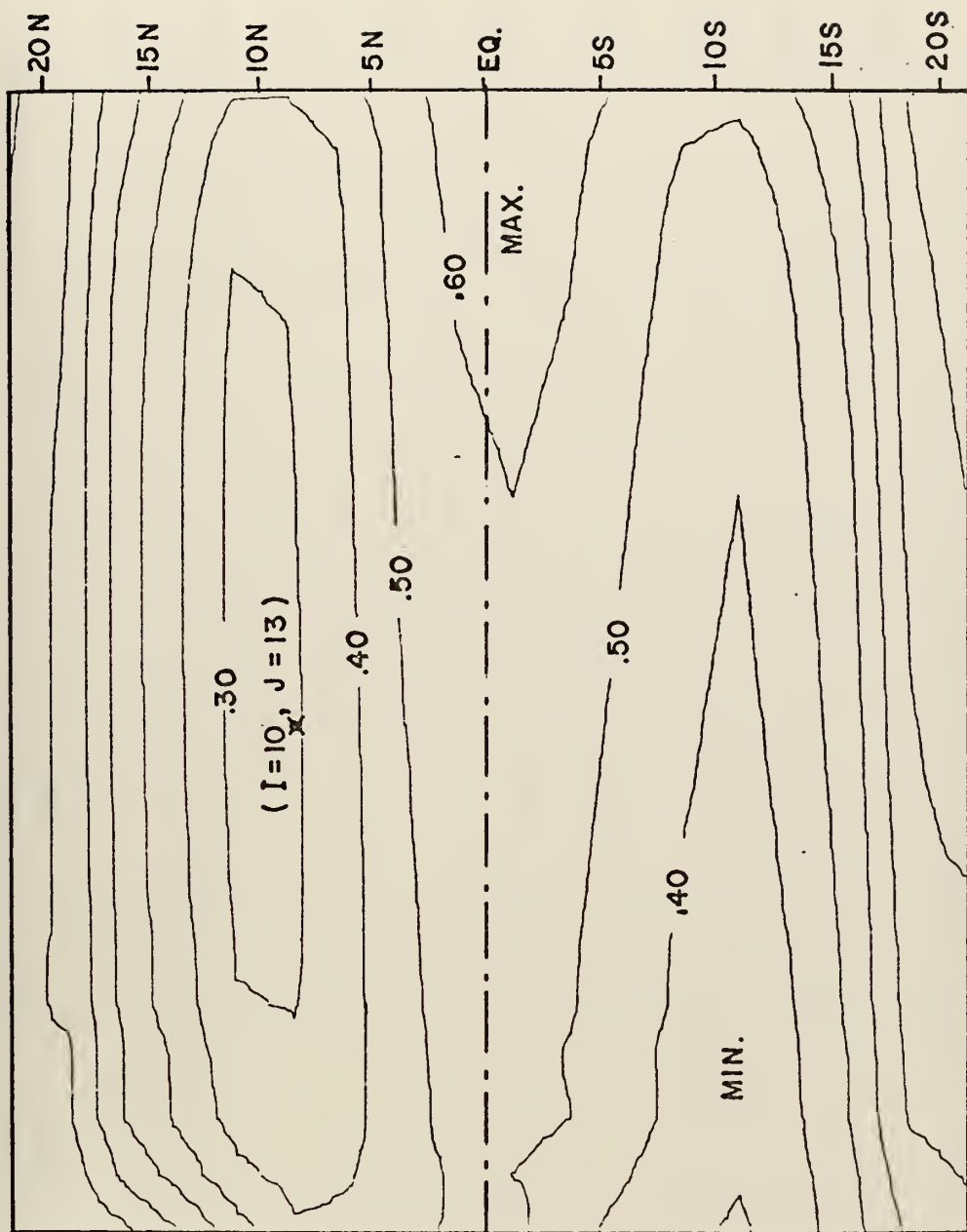


Figure 3.20. Horizontal cross section of salinity anomaly ($S^{\circ\text{‰}}$ = 34.‰) at 100 m after 30 years. The contour interval is 0.1‰. The point $I = 10$, $J = 13$ is the location of vertical salinity soundings that were used to find the salinity relaxation times.

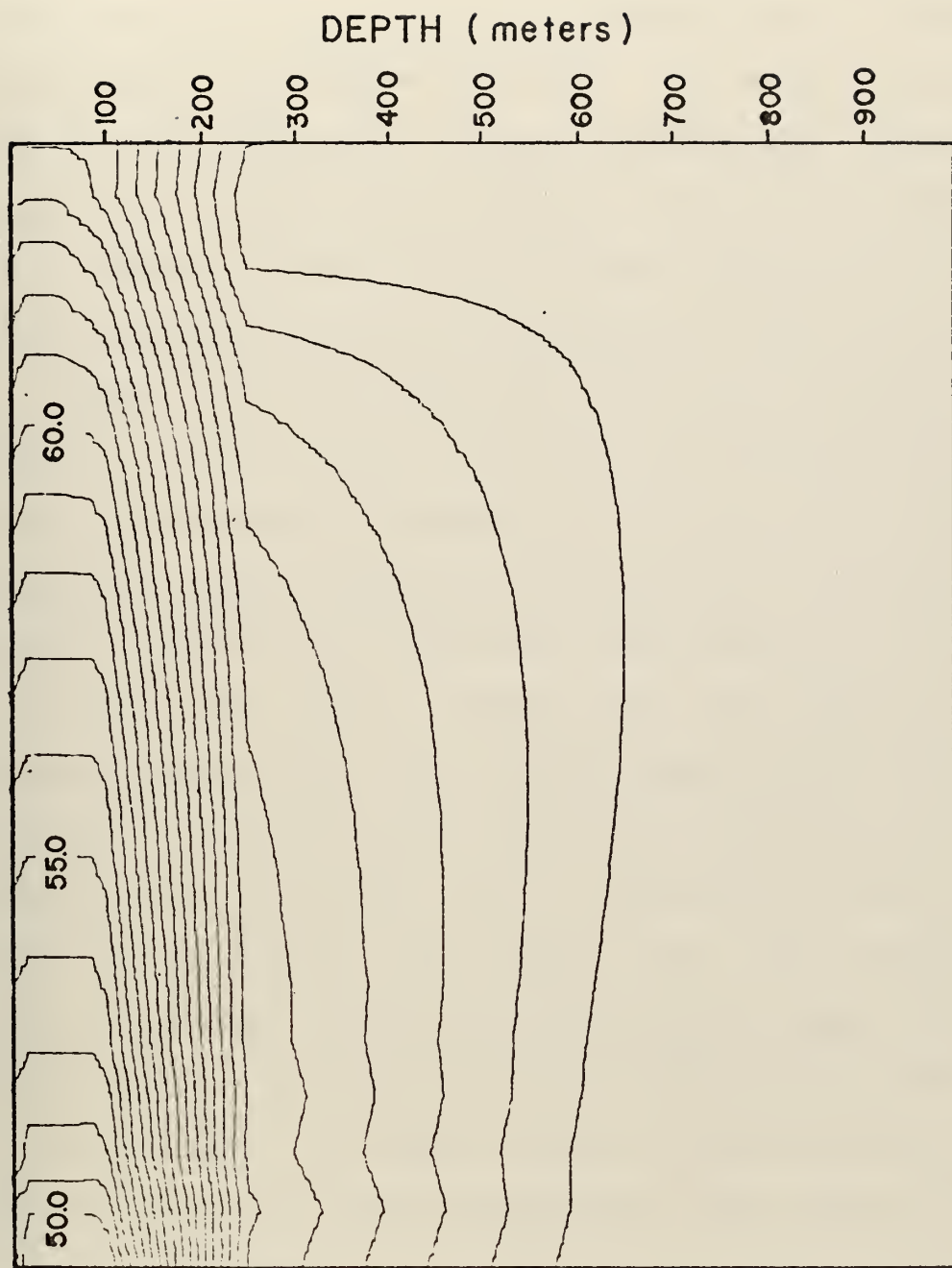


Figure 3.21 An E-W equatorial vertical cross section of salinity anomaly ($S\text{‰} - 34.\text{‰}) \times 100$.

these two minima a relative maximum centered at approximately 1 S formed due to the relative maximum in the prescribed downward flux of salt and a contribution due to vertical advection at the eastern boundary. The salinity minimum of the Northern Hemisphere was more intense than its southern hemispheric counterpart, a feature that must be related to the asymmetric surface stress τ_x (see figure 2.3) as all other boundary conditions were symmetric about the equator.

Figure 3.21, the equatorial E-W salinity anomaly cross section, further showed the effect of salinity advection. Since the prescribed surface flux of salt in the equatorial regions is upward, salinity must generally increase with depth. Thus, the top 300 meters are generally less saline than the deeper layers. Within this upper region of lower salinity water there is a shallow region between 50 m and 100 m of even less saline water due to the horizontal convergence of the meridional flux of fresh water from north and south of the equator (see figure 3.23). The existence of a core of minimum salinity above the axis of the countercurrent does not agree with the results of Krivelevich (1970) in his 40 layer model. He found a core of minimum salinity in the near surface region and reported that this agreed with observational data.

F. DENSITY STRUCTURE

Figure 3.22 is an equatorial E-W cross section of density anomaly ($\rho - 1.0$) $\times 1000$. Its similarity to figure 3.18, the corresponding cross section for temperature, and its

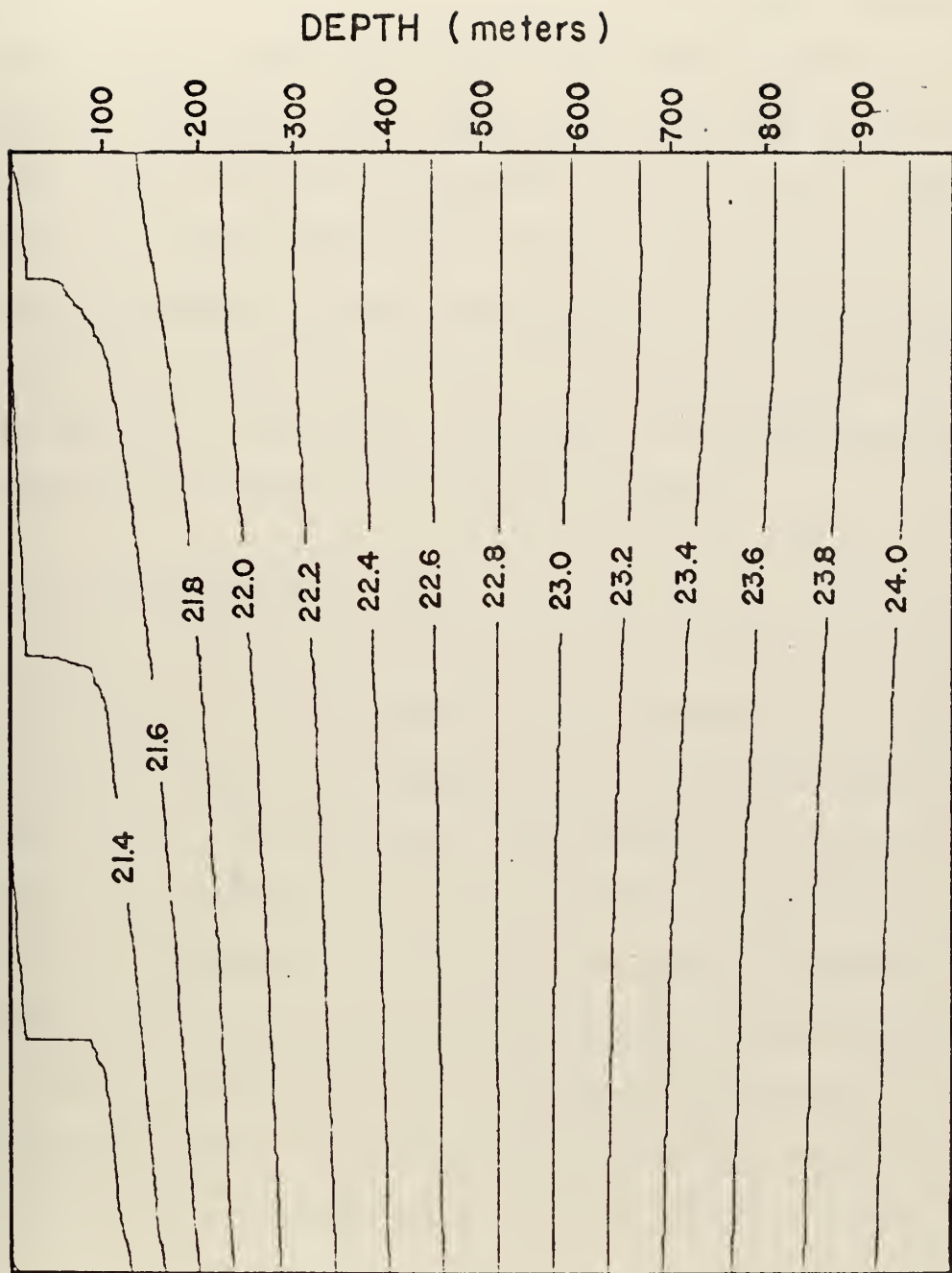


Figure 3.22 An equatorial E-W cross section of density anomaly $(\rho - 1.0) \times 1000$. The contour interval is 0.001 gm cm^{-3} .

dissimilarity to figure 3.21, especially in the upper 100 meters, suggested that temperature primarily determined the density structure. This same conclusion was reached by Krivelevich (1970) who used a nonlinear equation of state. Because of the strong dependence of density upon temperature and since the ocean was heated from above which tended to insure vertical stability, it was concluded that the convective adjustment process played only a minor role in determining the density structure. Convective adjustment was thought to be important only along the boundaries where significant vertical velocities existed.

G. MASS TRANSPORT

As mentioned previously, if the currents were nearly geostrophic in the vicinity of the equator, then the mass transport across the equator would be zero at each level. Figure 3.23, the transport streamfunction, showed however, there was transport from the Northern Hemisphere to the Southern Hemisphere at the surface with an opposite transport below. The dominant flow was a two cell circulation in which surface water was transported poleward in each hemisphere where it struck the boundaries, was forced to descend, and returned as deep water to the equator.

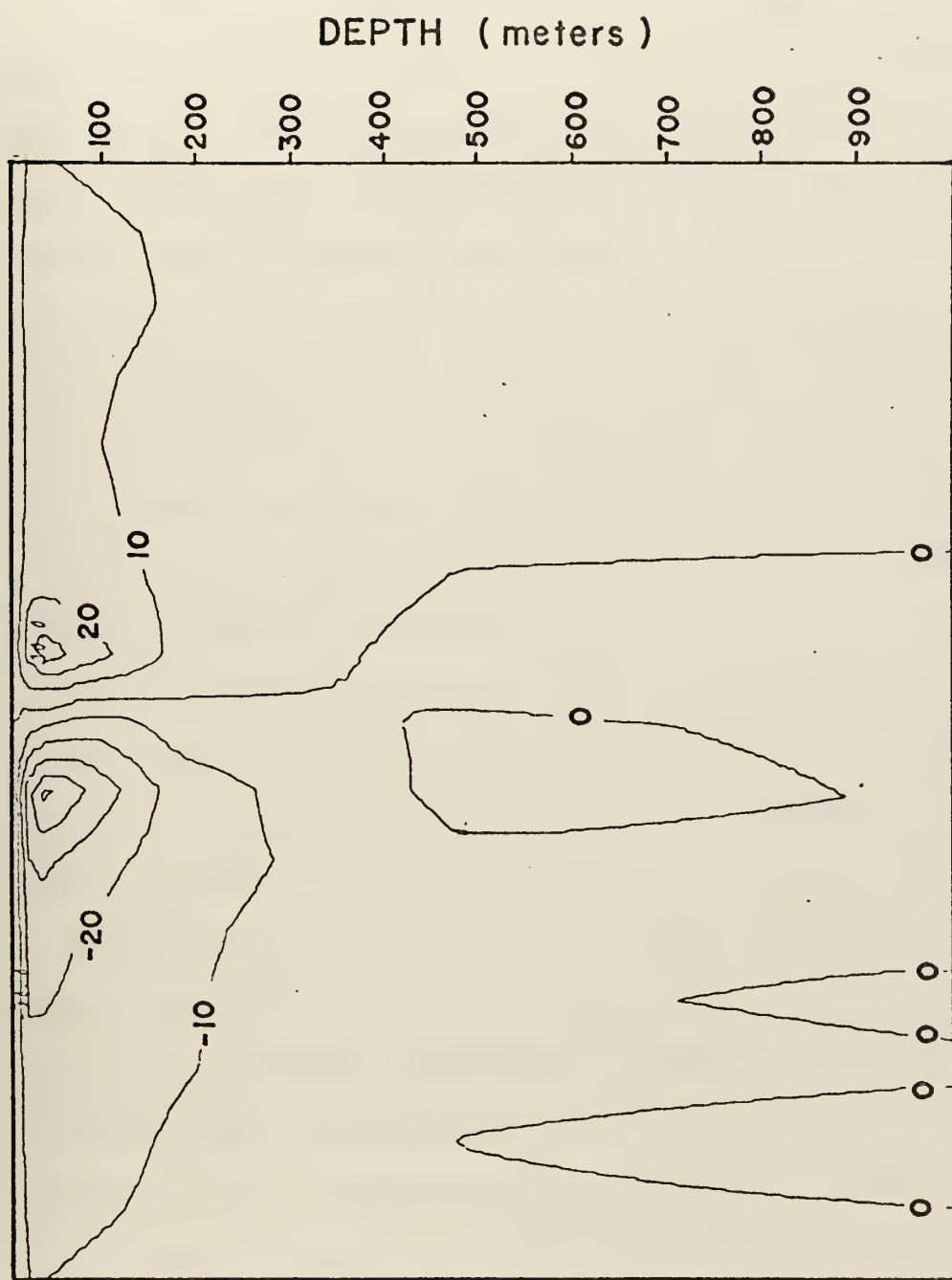


Figure 3.23 The transport streamfunction with a contour interval of $1.0 \times 10^4 \text{ cm}^2 \text{ sec}^{-1}$.

IV. CONCLUSIONS

The model is capable of simulating many features of the observed equatorial ocean flow such as vertical upwelling at the equator, Ekman divergence and surface mass transport towards each pole, and the existence of a subsurface countercurrent with a realistic meridional profile. The failure of the model to accurately resolve the countercurrent profile below 100 m was probably caused by using a vertical eddy diffusion coefficient for momentum, k_M , that was independent of vertical stability, vertical current shear, and depth. A better modeling of vertical mixing by using a variable k_M will probably give improved results.

The salinity pattern was shown to be strongly influenced by the model currents which were primarily wind driven, while the salinity distribution itself appeared to have little, if any, effect on the general current circulations.

The failure of the model to reach temperature or salinity steady state for the bottom layers over 30 years of time integration was not considered serious for an ocean forecasting model, where most of the variation in parameters tends to occur in the near surface layers. However, the slow thermal response time probably helped to prevent the formation of the deep isothermal layer and some means of accurately specifying the initial temperature profile is clearly needed.

REFERENCES

1. Arthur, R. S., 1960: A review of the calculation of ocean currents at the equator. Deep-Sea Res., 6, 287-297.
2. Bjerknes, J., 1966: A possible response of the atmospheric Hadley circulation to equatorial anomalies of temperature. Tellus, 18, 4, 820-829.
3. Bryan, K., 1969: Climate and the ocean circulation III. The ocean model. Mon. Wea. Rev., 97, 806-827.
4. Bryan, K., and M. D. Cox, 1968: A nonlinear model of an ocean driven by wind and differential heating: Part I. Description of the three-dimensional velocity and density fields, J. Atom. Sci., 25, 945-967.
5. Bryan, K., and M. D. Cox, 1968: A nonlinear model of an ocean driven by wind and differential heating: Part II. An analysis of heat, vorticity and energy balance. J. Atom. Sci., 25, 968-978.
6. Budyko, M. I., 1963: (Editor), Atlas teplovo balansa zemnogo shara (Guide to the atlas of the heat balance of the earth), Gidrometeoizdat, Moscow, 69 pp.
7. Charney, J. G., 1960: Non-linear theory of a wind-driven homogeneous layer near the equator. Deep-Sea Res., 6, 303-310.
8. Haney, R. L., 1971: A numerical study of the large scale response of an ocean circulation to surface heat and momentum. Ph. D. Thesis, University of California at Los Angeles, 191 pp.
9. Hellerman, S., 1967: an updated estimate of the wind stress on the world ocean. Mon. Wea. Rev., 95, 607-626; and Correction Notices, Mon. Wea. Rev., 95, 966 and 96, 63-74.
10. Knauss, J. A., 1960: Measurement of the Cromwell Current. Deep-Sea Res., 6, 265-286.
11. Knauss, J. A., 1966: Further measurements and observations on the Cromwell Current. J. Marine Res., 24, 205-239.
12. Krivelevich, L. M., 1970: Effect of water temperature and salinity on the formation of ocean currents at the equator. Oceanology, 10, 308-314.

13. Lambertson, W. R., 1972: A numerical investigation of the long-term transient behavior in a coupled atmosphere-ocean model. Ph. D. Thesis, Naval Postgraduate School, 193 pp.
14. London, J., 1957: A study of the atmospheric heat balance. Final Report, Contract No. AF19(122)-165, Department of Meteorology and Oceanography, New York University, 99 pp.
15. Manabe, S., 1969: Climate and the ocean circulation II. The atmospheric circulation and the effect of heat transfer by ocean currents. Mon. Wea. Rev., 775-805.
16. Munk, W. H., 1950: On the wind-driven ocean circulations. J. Met., 7, 79-93.
17. Veronis, G., 1960: An approximate theoretical analysis of the equatorial undercurrent. Deep-Sea Res., 6, 318-327.
18. Von Arx, W. S., 1964: An introduction to physical oceanography, Addison-Wesley, 118-139.

INITIAL DISTRIBUTION LIST

	No. Copies
1. Defense Documentation Center Cameron Station Alexandria, Virginia 22314	2
2. Library, Code 0212 Naval Postgraduate School Monterey, California 93940	1
3. Dr. R. L. Haney, Code 51Hy Department of Meteorology Naval Postgraduate School Monterey, California 93940	5
4. Lieutenant Byron Maxwell, USNR Environmental Prediction Research Facility Naval Postgraduate School Monterey, California 93940	5
5. Naval Weather Service Command Washington Navy Yard Washington, D. C. 20390	1
6. Commanding Officer United States Fleet Weather Central COMNAVMARIANAS, Box 12 FPO San Francisco, California 96630	1
7. Commanding Officer Fleet Weather Central Box 31 FPO New York, New York 09540	1
8. Director, Naval Research Laboratory Attn: Tech. Services Info. Officer Washington, D. C. 20390	1
9. Office of Naval Research Department of the Navy Washington, D. C. 20360	1
10. Commanding Officer Fleet Weather Central Box 110 FPO San Francisco, California 96610	1
11. Department of Meteorology, Code 51 Naval Postgraduate School Monterey, California 93940	1

12.	Department of Oceanography, Code 58 Naval Postgraduate School Monterey, California 93940	1
13.	Prof. George J. Haltiner Chairman, Department of Meteorology, Code 51Ha Naval Postgraduate School Monterey, California 93940	1
14.	Dr. R. L. Elsberry, Code 51Es Department of Meteorology Naval Postgraduate School Monterey, California 93940	1
15.	Dr. R. T. Williams, Code 51Wu Department of Meteorology Naval Postgraduate School Monterey, California 93940	1
16.	Prof. Dale F. Leipper Chairman, Department of Oceanography Naval Postgraduate School Monterey, California 93940	1
17.	Dr. J. A. Galt, Code 58G1 Department of Oceanography Naval Postgraduate School Monterey, California 93940	1
18.	Commanding Officer Fleet Numerical Weather Central Naval Postgraduate School Monterey, California 93940	1
19.	Commander Celia Barteau Fleet Numerical Weather Central Naval Postgraduate School Monterey, California 93940	1
20.	Dr. Jack Kaitala Fleet Numerical Weather Central Naval Postgraduate School Monterey, California 93940	1
21.	Lieutenant Commander W. Roger Lambertson Fleet Numerical Weather Central Naval Postgraduate School Monterey, California 93940	1
22.	Commanding Officer Environmental Prediction Research Facility Naval Postgraduate School Monterey, California 93940	1

23. Lieutenant James V. Sullivan, Jr., USN 1
Class 40
U.S.N. Destroyer School
Newport, Rhode Island 02840

24. Mrs. Olivera Haney 1
Environmental Prediction Research Facility
Naval Postgraduate School
Monterey, California 93940

25. Dr. W. L. Gates 1
The RAND Corporation
1700 Main Street
Santa Monica, California 90406

26. Dr. Richard Alexander 1
The RAND Corporation
1700 Main Street
Santa Monica, California 90406

27. Prof. Y. Mintz 1
Department of Meteorology
U.C.L.A.
Los Angeles, California 90024

28. Prof. A. Arakawa 1
Department of Meteorology
U.C.L.A.
Los Angeles, California 90024

29. Dr. Joseph Huang 1
NORPAX Project-T-28
Scripps Institution of Oceanography
P. O. Box 109
La Jolla, California 92037

30. Dr. F. Winninghoff 1
Department of Meteorology
U.C.L.A.
Los Angeles, California 90024

31. Dr. Tim Barnett 1
NORPAX Project-T-28
Scripps Institution of Oceanography
P. O. Box 109
La Jolla, California 92037

32. Dr. Kenzo Takano 1
Rikagaku Kenkyusho
Yamato-Machi
Saitama Pref. JAPAN

DOCUMENT CONTROL DATA - R & D

(Security classification of title, body of abstract and indexing annotation must be entered when the overall report is classified)

1. ORIGINATING ACTIVITY (Corporate author)		2a. REPORT SECURITY CLASSIFICATION Unclassified
Naval Postgraduate School Monterey, California 93940		2b. GROUP

3. REPORT TITLE

An Ocean Forecasting Model for the Equatorial Region

4. DESCRIPTIVE NOTES (Type of report and, inclusive dates)

Master's Thesis; September 1972

5. AUTHOR(S) (First name, middle initial, last name)

Byron Richard Maxwell

6. REPORT DATE September 1972	7a. TOTAL NO. OF PAGES 96	7b. NO. OF REFS 18
8a. CONTRACT OR GRANT NO.	9a. ORIGINATOR'S REPORT NUMBER(S)	
b. PROJECT NO.	9b. OTHER REPORT NO(S) (Any other numbers that may be assigned this report)	
c.	d.	

10. DISTRIBUTION STATEMENT

Approved for public release; distribution unlimited

11. SUPPLEMENTARY NOTES	12. SPONSORING MILITARY ACTIVITY Naval Postgraduate School Monterey, California 93940
-------------------------	---

13. ABSTRACT

A seven level primitive equation equatorial ocean model with temperature and salinity is integrated over a 30 year period to a quasi-steady state. Placement of four of the seven levels of the model in the first 100 meters gives sufficient vertical resolution to resolve most major features of equatorial oceans. The model equivalents of the South Equatorial Current, the Cromwell Current, vertical upwelling in the equatorial area, Ekman divergence of mass toward each pole, and a thermocline were all simulated.

A major conclusion was salinity probably has little effect on the general circulation patterns in the equatorial region. Additionally, the use of a vertical eddy diffusion coefficient for momentum that is dependent upon vertical stability, vertical current shear, and depth will probably be required to accurately model the vertical structure of the currents.

14 KEY WORDS	LINK A		LINK B		LINK C	
	ROLE	WT	ROLE	WT	ROLE	WT
Ocean						
Numerical						
Ocean Circulation						
Ocean Prediction						
Equatorial Ocean Model						

Thesis
M387 Maxwell 139066
c.1 An ocean forecasting
model for the equatorial
region.

Thesis
M387 Maxwell 139066
c.1 An ocean forecasting
model for the equatorial
region.

thesM387
An ocean forecasting model for the equat



3 2768 002 12555 1
DUDLEY KNOX LIBRARY